Development of a 2D Boundary Element Method to model Schroeder Acoustic Diffusers

Andrew Lock 098911

October 2014

Supervisor: Dr Damien Holloway

Submitted in partial fulfilment of the requirements for the Degree of Bachelor of Engineering with Honours, University of Tasmania

This Thesis to the best of my knowledge and belief contains no material published or unpublished that was written by another person, nor any material that infringes copyright, nor any material that has been accepted for a degree or diploma by University of Tasmania or any other institution, except by way of background information and where due acknowledgement is made in the text of the thesis.

This Thesis is the result of my own investigation, except where otherwise stated. Other sources are acknowledged in the text giving explicit references. A list of references is appended.

Signed:

Date:

I hereby give consent for my Thesis to be available for photocopying, inter-library loan, electronic access to UTAS staff and students via the UTAS Library, and for the title and summary to be made available to outside organisations.

Signed:

Dated:

Abstract

Acoustic diffusers are used in the treatment of critical listening environments, and their performance is efficiently predicted by the Boundary Element Method (BEM). Schroeder diffusers are highly effective due to diffusion lobes produced by phase delays from different depth wells. The initial aim of this work was to further develop and optimise a 2D BEM code by Rocchi & Smith (2013) for modelling Schroeder diffusers, through improved computation methods and algorithms. In particular, an analytical integral of the Green's function for diagonal matrix elements was implemented, and the numerical integration methods for all other elements was refined. Computation time decreased by a factor of 50, and average error for the test case of an infinite cylinder reduced by a factor or 200. Intelligent discretisation methods also reduced the number of elements needed for accurate results. The performance of Quadratic Residue Diffusers (QRDs) and QRD modifications was investigated, including the effects of design dimensions, acoustic field type and repeating periods. A systematic approach was used to model the performance of over 40 common diffusers. The superior performance of Quadratic Residue Diffusers (QRDs) with larger sequences was confirmed when modelled in a plane wave acoustic field. However, the performance of QRDs with large sequences decreased significantly when modelled in a point source acoustic field. Preliminary tests of a novel fractal QRD design displayed promising results.

Acknowledgements

Firstly, I would like to express my sincere thanks to Dr Damien Holloway, not only for his knowledge, enthusiasm, and generous time on this project, but also for his wider contribution to our undergraduate studies.

To my parents, Sally and Chris. Thank you for your constant support throughout my education, in particular during this final year.

Finally, to the lads of the Annex. My time here would not have been nearly as productive nor enjoyable without your good company.

Contents

I Background **1**

1 Introduction **2**

1.1 Objective and scope 3

1.2 Structure 4

2 Literature Review **5**

2.1 Acoustic waves 5

2.2 Acoustic field types 6

2.2.1 Plane wave incident field 6

2.2.2 Point source incident field 7

2.3 Surface effects 7

2.3.1 Absorption 7

2.3.2 Reflection 8

2.3.3 Diffusion 8

2.3.3.1 Diffusion coefficient 10

2.3.3.2 Scattering coefficient 11

2.3.4 Comb filtering 12

2.4 Acoustic diffusers 13

2.4.1 Development 13

2.4.2 Curved and cylindrical surfaces 14

2.4.3 Schroeder diffusers 14

2.4.3.1 Maximum Length Sequence diffusers 15

2.4.3.2 Quadratic Residue Diffusers 16

2.4.3.3 Primitive Root Diffusers 19

2.4.4 State-of-the-art on QRD design 20

2.4.4.1 Fractal diffusers 20

2.4.4.2 Modulated QRDs . . . 21
2.4.4.3 Three-dimensional Schroeder Diffusers . . . 22
2.5 BEM . . . 22
2.5.1 Conditions and Limitations . . . 23
2.5.1.1 Continuous surface geometry . . . 23
2.5.1.2 Non-unique solutions . . . 23
2.5.2 State-of-the-art on BEM modelling . . . 24
2.5.2.1 Thin panel solution to BEM modelling . . . 24
2.5.2.2 Three dimensional modelling with the BEM . . . 25

II BEM Code Development and Optimisation 26

3 MATLAB BEM Overview 27
3.1 Acknowledgements . . . 27
3.2 Executing the BEM code . . . 28
3.2.1 BEM code flowchart . . . 29

4 BEM Theory 30
4.1 BEM assumptions . . . 30
4.2 Wave theory . . . 31
4.3 Incident sound field . . . 31
4.4 Rigid body boundary condition . . . 32
4.5 Green's second identity . . . 33
4.6 Discretisation of the boundary . . . 33
4.7 The Hankel functions . . . 34
4.8 Integration methods . . . 37
4.8.1 Numerical integration . . . 37
4.8.2 Analytical integration . . . 38

5 BEM Code Development and Optimisation 40
5.1 Techniques . . . 40
5.1.1 Improvement of receiver solution calculation . . . 40
5.1.2 Code structure . . . 40

5.1.3 [M] and [L] coefficient matrix creation 41
5.1.4 Element edge size refinement 43
5.1.5 Fix for non-unique BEM solutions 46
5.2 Code Optimisation and Development Results 48
5.2.1 Overview 48
5.2.2 Comparison to analytic solution 48
5.2.3 Comparison to published diffusion data 50
5.2.4 Timing improvements 53
5.2.5 Element size, accuracy and convergence 56
5.2.5.1 Thin panel errors 57
5.2.5.2 Solution convergence 58
5.2.5.3 Other effects 61
5.2.6 Element size guidelines 61
5.3 BEM code development and optimisation conclusion 62
5.3.1 Potential for further work 63

III Investigation of Schroeder Diffuser Performance 64

6 Investigation overview 65
6.1 Investigation scope and objectives 65
6.2 Model details 66

7 Diffuser Performance Results and Discussion 67
7.1 Performance of classical QRDs 67
7.1.1 Effect of prime number N 68
7.1.2 Effect of acoustic field type 69
7.1.3 Frequency range of diffusion for $N = 7$ QRDs 69
7.1.4 Effect of phase shifted sequences 71
7.2 QRD fractals 72
7.3 Well divider panel thickness 74

8 Conclusion and key findings 77
8.0.1 Potential for further work 78

Bibliography **79**

A Additional results **82**

A.1 QRD performance results 82

A.2 Acoustic field comparison results 87

B Additional details **88**

B.1 BEM Program Steps 89

B.2 A concise derivation of Green's second identity from the divergence theorem 90

B.3 Diffuser dimensions 93

B.4 Specifications of Computer used in code timing 93

B.5 Gaussian quadrature weights and abscissae 94

List of Figures

2.1.1 Illustration of pressure waves at a snapshot in time (Everest & Pohlmann, 2009) [11] 5
2.1.2 Superposition of multiple sine waves. 6
2.3.1 Sound wave reflection 8
2.3.2 Incident wave spatially diffused 9
2.3.3 Cylindrical wave reflected from a Schroeder diffuser calculated using an FDTD model. 9
2.3.4 Comparison of c_d, c_p and c_n for an $N = 23$ QRD. 11
2.4.1 Example of energy lobe diffraction pattern from $N = 7$ QRD at 4 times f_0. 15
2.4.2 Cross section of N=7 MLS diffuser. 16
2.4.3 Example of $N = 7$ QRD in single and repeating periods. 17
2.4.4 An $N = 7$ QRD array of multiple repeating periods. 19
2.4.5 An $N = 7$ QRD design with two levels of fractals nested within each well. 21
2.4.6 QRD and diffusion pattern for one-dimensional and two-dimensional QRDs. 22
2.5.1 A two-dimensional diffuser modelled using a three-dimensional BEM. . . . 25

3.2.1 Flowchart of current BEM code. 29

4.7.1 Absolute value of Hankel functions of constant k and increasing r. 36

5.1.1 Surface pressures of an infinite square column in a point source acoustic field. 44
5.1.2 QRD surface pressure gradient magnitude 45
5.1.3 Infinite square column discretisation with and without edge refinement. . 46
5.1.4 QRD model with hollow cavity to check for non-unique solutions. 47
5.2.1 Diagram of diffusion model from an infinite cylinder. 49
5.2.2 Diffusion from a cylinder due to a plane wave. 49
5.2.3 Comparison of diffusion lobe positions (dB) for an $N = 7$ QRD. 51
5.2.4 Comparison of normalised diffusion coefficients between values published by Cox & D 'Antonio [7] and BEM program. 52

5.2.5 Convergence of diffusion coefficient at 2500 Hz for QRD as modelled in Figure 5.2.4 52
5.2.6 Timing comparison between original and optimised code. 54
5.2.7 Comparison of solution time and convergence from 3 BEM code versions. 54
5.2.8 Example of convergence testing with varying panel width with for $N = 7$ QRD. 57
5.2.9 Maximum element size for which convergence errors are not dominated by thin panel errors. 58
5.2.10 Convergence study with normalised element length e_n. 60

7.1.1 Performance of QRD arrays of variable N in a plane wave incident field. . 68
7.1.2 Comparison of QRD performance in different acoustic fields. 69
7.1.3 Performance data for $N = 7$ QRD arrays with varying P. 70
7.1.4 Comparison of regular and phase shifted QRD performance. 71
7.2.1 Four fractal-type QRD designs tested for diffusion frequency bandwidth. . 73
7.2.2 Comparison of three fractal designs and regular QRD performance. 73
7.3.1 Effect of thin panel width on diffuser performance 75

A.1.1 QRD diffusion data. 86
A.2.1 Comparison of different acoustic fields for QRDs of comparable w_T and varying Nw_T. 87

List of Tables

2.4.1 Quadratic Residue Sequence calculation example for $N = 7$ 16
2.4.2 Primitive root Sequence calculation example for $N = 7$, $r = 3$ 20
2.4.3 Example of a regular and phase shifted Quadratic Residue Sequence . . . 21

3.2.1 BEM code subroutines 28

5.1.1 r threshold values and Gaussian Quadrature points. 42
5.2.1 Comparison of receiver pressure error when compared to an analytic solution 50
5.2.2 Solution time improvements breakdown 55
5.2.3 QRD details for convergence testing, as shown in Figure 5.2.10 59

B.1.1BEM program steps 89
B.3.1Table of QRD dimensions for test as shown in Figure 7.1.1 93
B.4.1Specifications of computer used in code timing 93
B.5.1Gaussian Quadrature weights and abscissae 94

Nomenclature

f	Frequency (Hz)
f_0	Design frequency (Hz)
f_c	Critical frequency (Hz)
λ	Wavelength (m)
λ_c	Critical wavelength (m)
k	Wavenumber (m^{-1})
ϕ	Acoustic potential
p	Pressure (Pa)
BEM	Boundary Element Method
QRD	Quadratic Residue Diffuser
PRD	Primitive Root Diffuser
N	Prime number used in QRD and PRD sequence
r	Primitive root of N
$d_{\max}$	Maximum well depth of QRD (m)
w	Width of QRD well (m)
$w_{_P}$	Width of well dividing panel (m)
$w_{_T}$	Width of combined well and panel divider (m)
$Nw_{_T}$	Period width (m)
P	Number of periods of sequential diffuser in array
$c_{d,\psi}$	Diffusion coefficient for incident angle ψ
$c_{r,\psi}$	Reference diffusion coefficient for incident angle ψ
$c_{n,\psi}$	Normalised diffusion coefficient for incident angle ψ
s	Scattering coefficient
α	Absorption coefficient
ψ	Angle of sound wave from normal to diffuser
r	Distance between two elements (m)
ka	Dimensionless radius of cylindrical diffuser
kr	Dimensionless radius of off-surface receivers
e	Element size (m)
$e_{\max}$	Maximum element size (m)
e_{edge}	Maximum element size adjacent to edge (m)

Part I

Background

Chapter 1

Introduction

An acoustic diffuser is an object or surface profile designed to provide a diffuse reflection from an incident sound wave. While nearly all reflective surfaces will offer some degree of diffusion, an acoustic diffuser is designed to produce high levels of diffusion or specific diffusion characteristics, often for a design application or frequency range. Diffusion can be either temporal (time-related) or spatial, and is a useful tool in the in acoustic treatment of spaces such as critical listening rooms and performance spaces, often to create a more even sound field or to avoid strong reflections [7]. Where traditionally acoustic absorbers have been used to avoid undesirable acoustic effects, there is a growing trend towards the use of diffusers instead [7], and this has increased the need to accurately model their performance.

The diffusion produced by an object in an incident acoustic field can be described by the sound pressure levels at points around the object, either as done experimentally by Wiener [31] (1947) or through theoretical analysis. Methods of analysis include analytical solutions for some simple common geometries such as that of a cylinder published by Morse [21] (1986), Finite Element Analysis, Finite-Difference Time Domain (FDTD) method, and the Boundary Element Method (BEM). Theoretical predictions are used in the design and optimisation of acoustic diffusers, as well as predicting the performance of existing diffuser shapes and surfaces.

Two final year engineering students, Nicholas Smith [28] (2013) and Luca Rocchi [23] (2013), developed a MATLAB[1] implementation of the BEM to model the performance of acoustic diffusers. Their findings aligned with Cox & D'Antonio [7], showing that for many applications, the BEM is a superior method for diffuser analysis when compared to other methods, in particular, Finite Element Analysis.

[1]MATLAB is a numerical computing environment and programming language.

1.1 Objective and scope

The initial aim of this work is to further develop and document the BEM program written by Rocchi and Smith. Accuracy and timing improvements to the BEM code are achieved through.

- correction of errors in the original BEM code;
- analytical integration of diagonal matrix terms (see Chapter 4.8.2);
- variation in the number of Gaussian Quadrature integration points used in matrix term calculations (see Chapter 4.8.1);
- code restructuring and in some cases complete replacement, to increase speed and make use of MATLAB's built-in acceleration features (see Chapter 5.1.2); and
- element size refinement in critical locations such as edges (see Chapter 5.1.4).

Increased functionality was also added, including:

- a formula derived from a detailed convergence study to determine the required element size for a given frequency, geometry and level of accuracy;
- MATLAB functions written to automatically create QRD geometry with variable dimensions and features (see Chapter 2.4.3.2);
- the capability to model a point source incident sound field in addition to a plane wave field (see Chapter 4.3);
- frequency band modelling and averaging; and
- the calculation of the diffusion coefficient, reference plate diffusion coefficient and normalised diffusion coefficient (see Chapter 2.3.3.1);

A detailed validation and convergence analysis was completed, and documentation accompanies this code to increase its usability. The second aim of this work is to use the the developed code to predict the performance of Schroeder diffusers, with a focus on the advantages provided by increased efficiency and accuracy.

1.2 Structure

This study is divided into three distinct parts. Part I introduces the topic, and discusses related concepts and past research. Part II outlines the development of a MATLAB BEM code used to model the scattering from objects within an acoustic field. Part III is an investigation into the diffusive properties of Schroeder diffusers using the BEM code. A brief description of each chapter is included below.

Chapter 2: This chapter contains a review of current literature relevant to the topic, including fundamental acoustic principles, the BEM, and common diffuser designs and theory. Particular detail is paid to QRDs including recent developments in QRD design.

Chapter 3: An introduction is given to the MATLAB implementation of the BEM, including descriptions of the code structure and instructions on executing the code.

Chapter 4: A detailed derivation of the BEM is presented, and the steps used to solve a discretised form of the BEM are described.

Chapter 5: The development of the BEM code during this work is documented, including the methods used to increase efficiency and accuracy. The code is thoroughly tested, and the improvements are quantified. From a study of error and convergence, an empirical equation is derived for the estimated accuracy when using the code to model Schroeder diffusers.

Chapter 6: The scope of the investigation into Schroeder diffusers is outlined, and the details used during diffusion modelling are listed.

Chapter 7: Results from Schroeder diffuser BEM models are presented and discussed. The results are compared to the traditional design equations that describe the performance of these diffusers.

Chapter 8: Conclusions and key findings are summarised, and further research is suggested.

Chapter 2

Literature Review

From published literature, this chapter will explain some of the fundamental acoustic principles including basic wave theory, absorption, reflection and diffusion. Some common diffuser shapes will then be discussed, with particular attention to Schroeder diffusers. Recent developments in Schroeder diffuser design such as repeating periods, modulated periods and fractals are discussed, along with state-of-the-art in BEM acoustic modelling.

2.1 Acoustic waves

An acoustic wave is the movement of pressure waves through an elastic medium, which for most cases, and the focus of this work, is air. Figure 2.1.1 shows an illustration of pressure waves at a snapshot in time, with the corresponding graphical representation. The speed of sound c in air at normal temperature is $c \approx 343$ m/s [11].

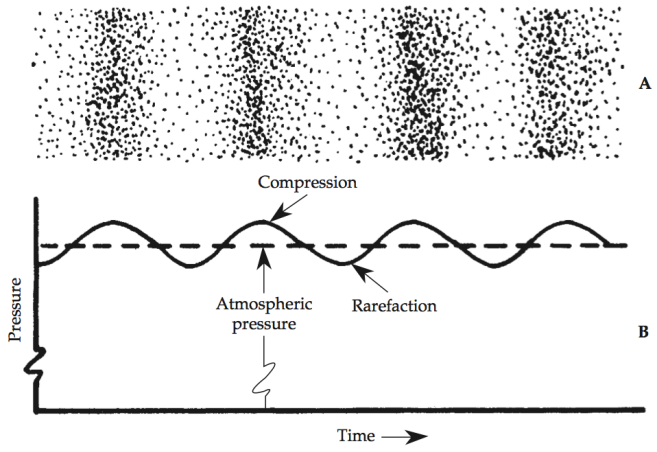

Figure 2.1.1: Illustration of pressure waves at a snapshot in time (Everest & Pohlmann, 2009) [11]

Pressure waves can be considered sinusoidal with respect to time and distance. An

acoustic field is usually a superposition of pressure waves of different amplitudes and frequencies, as shown in Figure 2.1.2. This concept also applies to the interaction between incident and diffracted waves, and is the cause of comb filtering, as discussed in Chapter 2.3.4.

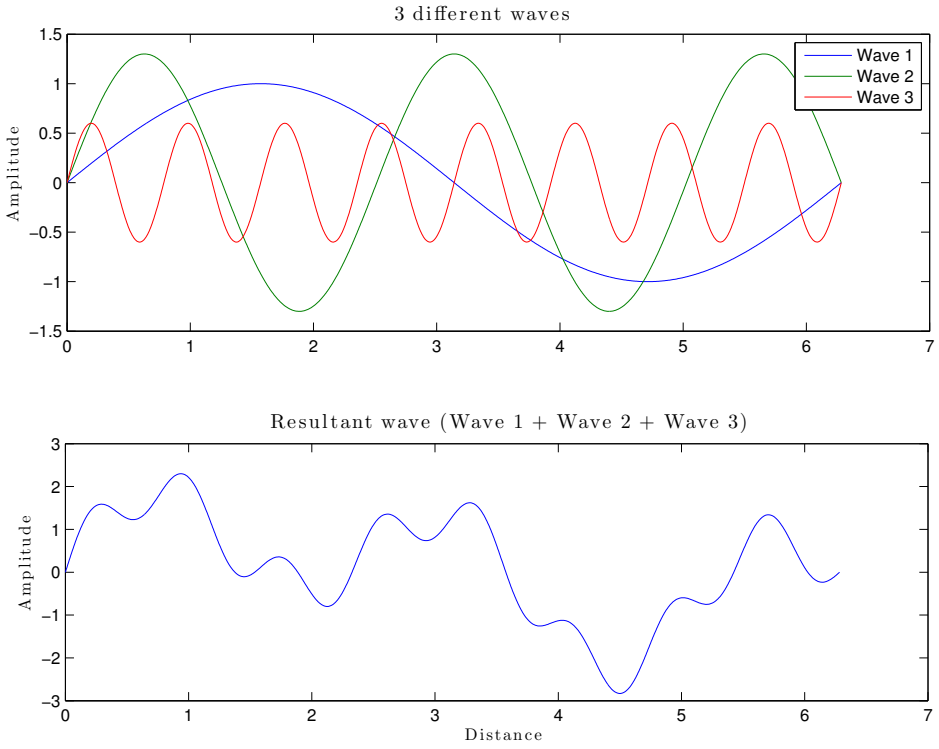

Figure 2.1.2: Superposition of multiple sine waves.

2.2 Acoustic field types

The acoustic field in most environments consists of a mixture of incident sound from one or more sources, and reflections from the ground, walls or objects within the acoustic field. For the purposes of analysis during this investigation, the incident acoustic field is simplified into two categories, a plane wave and point source, both of which ignore the effect of reflections.

2.2.1 Plane wave incident field

A plane wave incident field describes an acoustic field where, at any point in time, pressure varies in one dimension only. While this exact field type rarely exists in actuality, it

is a reasonable approximation for a source at much larger distance from an object than the object's dimensions normal to the wave direction. On a two dimensional application in x, y co-ordinates, a plane wave approaching from the positive y direction can be assumed to have constant pressure P in the x direction at any point in time, $\frac{\partial P}{\partial x} = 0$. The rate at which pressure changes in the y direction is related to the amplitude and frequency of the plane wave (see Chapter 4.3).

2.2.2 Point source incident field

For situations where the distance between an acoustic source is comparable to the dimensions of the object or receivers, the wavefront cannot be assumed to be planar. A point source incident field represents an acoustic source originating from a singular point within the sound field. For three dimensional applications, pressure waves radiate spherically, whereas for two dimension applications, waves radiate cylindrically from the source location. At any point in time, the pressure at a point is relative to the distance from the source only, or $\frac{\partial P}{\partial \theta} = 0$ where θ is the angle between receiver and source (see Chapter 4.3). The representation of a source originating from a single point results in a theoretical pressure approaching infinity at the source location. For this reason the acoustic field cannot be defined at the source location (see Chapter 4.7).

2.3 Surface effects

2.3.1 Absorption

Sound absorption is the reduction in energy of a sound wave due to the presence of an object in the sound field. This process involves the transmission of sound energy into the object, and the sound wave losing energy during the interaction with the fluid boundary layer across the object [7]. An example of an environment with very little sound absorption is an empty church, where most surfaces are highly efficient reflectors and minimal energy transferred to the wall medium. Conversely, recording studios and anechoic chambers are designed to have very high levels of absorptivity, where acoustic energy is absorbed by acoustic absorbers such as baffles. A room with 100% absorption would resemble an open outside environment, where none of an incident sound wave is reflected [11]. Absorbers, often combined with diffusers, are useful tools in the acoustic treatment of spaces.

The absorption properties of a material or surface are described by the absorption coefficient α, defined as the ratio of acoustic energy absorbed by a material to the incident wave energy [11]. The absorption coefficient is a function of frequency, and is usually represented as a value for the average of all incident angles, representing absorption from a diffuse sound field. An absorption coefficient of $\alpha = 1$ represents 100% absorption of incident acoustic energy by the material or surface, and $\alpha = 0$ represents a perfect reflector with no absorption.

2.3.2 Reflection

A perfect reflector is one that reflects an entire incident sound wave at an angle equal to that of incidence [7], as seen in Figure 2.3.1. Just as with light reflection, the virtual position of reflected sound is a position behind the reflector [11]. Most surfaces offer some absorption as well as reflection, with the reflected wave having a smaller amplitude than the incident wave. It should be pointed out that considering sound as a ray as in Figure 2.3.1 is a simplification; it is really a diverging wave with a spherical wavefront and decreasing energy obeying an inverse square law ($E \propto 1/r^2$) [11].

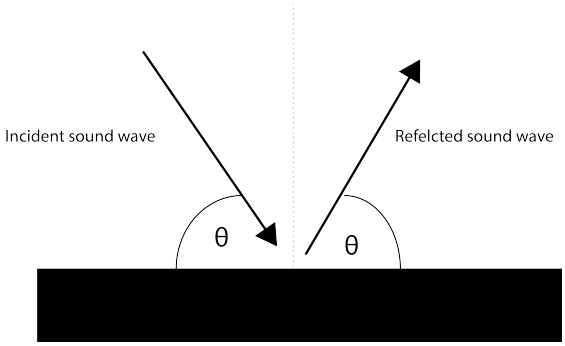

Figure 2.3.1: Sound wave reflection

2.3.3 Diffusion

Sound diffusion is the process of 'diffusing' sound waves within a space to provide a more even sound distribution [11]. Where a perfect reflector would reflect an incidence wave in one direction only, a perfect diffuser would reflect an incident wave from any angle evenly in all directions [**?**], as shown in Figure 2.3.2. Note that the term 'perfect' does not necessarily represent the most desirable diffusion [**?**]. A sound wave can also

be diffused temporally, or in respect to time as is shown for a transient wave in Figure 2.3.3. The rationale behind using acoustic diffusers to treat an acoustic space may be

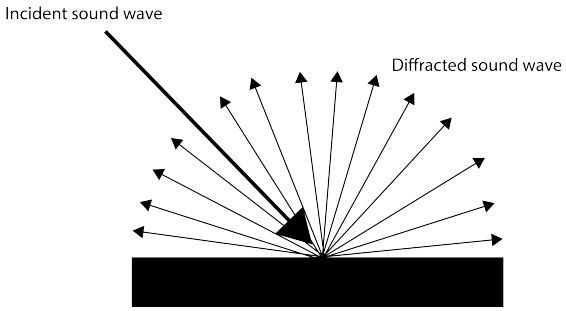

Figure 2.3.2: Incident wave spatially diffused

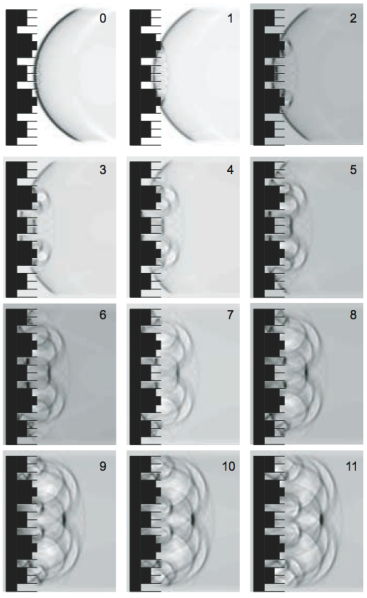

Figure 2.3.3: Cylindrical wave reflected from a Schroeder diffuser calculated using an FDTD model. From Cox & D'Antonio p. 36 [7].

to reduce strong reflections, to reduce the effect of comb filtering (discussed in Chapter 2.3.4), or provide a more even sound field [7]. Wenger Corporation [1] recommend installing acoustic diffusers in the front third of a performance space to help project sound towards the audience, and Cox & D'Antonio [7] recommend sound diffusers on the rear walls of performance spaces to avoid strong transient reflections. The diffuse properties of a space can be assessed through a measurement of the sound field in different locations, and through measurement of the temporal response of a transient sound wave [7].

Two indicators of the performance of a diffuser are the scattering coefficient and the diffusion coefficient; the scattering coefficient is an indication of the ability of a surface

to reduce the sound wave energy in the spatial reflection direction, whereas the diffusion coefficient is a measure of the uniformity of the spatial reflection across all directions [7].

2.3.3.1 Diffusion coefficient

The diffusion coefficient c_d is a recent development in the characterisation of a surface's diffusion properties, as published in the Audio Engineering Society (AES) standard AES-4id-2001 (r2007) [3]. It is a single figure measure of the uniformity of scattering for a surface at a particular frequency and incident angle. The AES standard states that the diffusion coefficient should be calculated as averaged one-third octave bandwidths to smooth local variations [7]. The diffusion coefficient is

$$c_{d,\psi} = \frac{\left(\sum_{i=1}^{n} 10^{L_i/10}\right)^2 - \sum_{i=1}^{n} \left(10^{L_i/10}\right)^2}{(n-1)\sum_{i=1}^{n} \left(10^{L_i/10}\right)^2} \tag{2.1}$$

where n represents the number of receivers, L_i the set of pressure levels in decibels from the receivers and ψ the source angle of incidence. The diffusion coefficient can be calculated in two or three dimensions and from experimental measurements or modelling, provided each receiver position samples an area of the same size. [7]

While the diffusion coefficient $c_{n,\psi}$ provides a measure of the uniformity of scattering, it does not provide a measure of the increase in scattering when compared to a flat surface. This is particularly important at low frequencies, where a flat surfaces can act as a point source and provide high levels of diffusion [7]. For this reason, the diffusion coefficient is normalised with reference to a flat surface of similar dimensions. The normalised diffusion coefficient $c_{n,\psi}$ is defined as

$$c_{n,\psi} = \frac{c_{d,\psi} - c_{r,\psi}}{1 - c_{r,\psi}} \tag{2.2}$$

where $c_{d,\psi}$ is the diffusion coefficient for the test sample, and $c_{r,\psi}$ is the diffusion coefficient for a reference flat surface of the same dimensions as the test sample, both calculated using Equation (2.1).

The AES standard provides recommendations for the number of receivers, receiver locations and radius from the diffuser and the source location. For two dimensional

diffusion modelling the standard recommends a source location of 5 m from the test sample, and receivers at least every 5° around a 180° arc with radius 10 m from the test sample. Unless otherwise stated, these AES recommendations will be followed in this study for diffusion modelling and calculation of the diffusion coefficient, with the exception that receivers will be placed every 0.5° around the test sample. Negative values for diffusion coefficients are possible, in particular at low frequencies when a plane surface of comparable size to wavelength exhibits high diffusion properties. Cox & D'Antonio [7] recommend displaying these as 0. However, they will be kept as negative values during this work in the interest of data preservation and model comparisons.

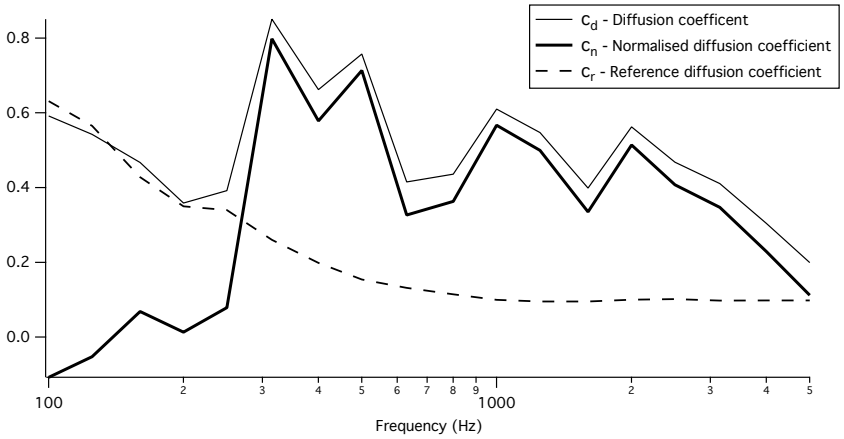

Figure 2.3.4: Comparison of c_d, c_p and c_n for a $N = 23$ QRD. $P = 2$, $f_0 = 500$ Hz, $Nw_T = 2.07$ m, $\psi = 0°$.

2.3.3.2 Scattering coefficient

Another coefficient used in the characterisation of diffusion properties is the scattering coefficient s. While the diffusion coefficient is a measure of the uniformity of scattering, the scattering coefficient is a measure of the ratio of energy reflected in the specular reflection direction, to the total reflected energy. The scattering coefficient is published in international standards number ISO 17497-1 [2], and can be represented as

$$s = 1 - \frac{E_{\text{spec}}}{E_{\text{total}}}, \tag{2.3}$$

where E_{spec} is the energy diffused in the specular direction, and E_{total} is the total reflected energy. The scattering coefficient value is averaged from all random incident angles and is therefore not a function of incidence angle, unlike the diffusion coefficient. It is worth

noting that the total reflected energy does not include sound energy absorbed by the material, expressed for an incident wave of unit energy as

$$E_{\text{total}} = 1 - \alpha_s \,,$$

and similarly, the specular reflected energy can be described as

$$E_{\text{spec}} = (1 - \alpha_s)(1 - s) \,,$$

where α_s is the absorption coefficient of the test sample.

The scattering coefficient is most commonly used when modelling reverberant fields such as indoor acoustics through geometrical room modelling, and is therefore usually calculated through experimentation at many incidence angles [11]. ISO 17497-1 describes the method used for experimental calculating of the scattering coefficient.

The diffusion coefficient is the most important parameter for diffuser design [11] and is therefore the coefficient used in this work, but it is worth considering that both the diffusion coefficient and the scattering coefficient can be of use to describe the scattering properties of a test sample.

2.3.4 Comb filtering

Comb filtering in acoustics is the effect of certain frequencies becoming amplified, while others are reduced, due to the interaction of a direct sound wave and its reflection from a surface. The reflection causes a time delay of the direct sound due to the increased distance it must travel, and when mixed with the direct sound can cause constructive and destructive interference [11]. It is a feature of steady-state sources, and is generally not considered for transient sound sources such as speech [11]. Occurring often due to large flat reflective surfaces, it should be avoided in critical listening rooms such as performance spaces and recording studios [7]. Treatment with absorbers and diffusers can greatly reduce the effect of comb filtering, where it may still occur but in a more randomised manner [7]. Reducing the effect of comb filtering can be a strong motive for the installation of diffusers in critical listening spaces.

2.4 Acoustic diffusers

2.4.1 Development

There are many different of types of diffusers and diffuser purposes, including those designed to scatter sound spatially or both spatially and temporally, as well as those designed for three-dimensional diffusion (commonly used on ceilings), and two-dimensional diffusion (commonly used on walls). The structural and architectural aspects of indoor spaces will affect their diffusion characteristics, and certain features such as circular pillars (see Chapter 2.4.2) can offer high diffusion properties [11]. Diffusers can be installed to further improve the diffusion properties when needed. Diffusers are most commonly rectangular panels with a surface profile designed to provide certain diffusion characteristics, but may also be convex shapes or other protruding geometries.

Manfred Schroeder is considered to have made the most substantial breakthrough in diffuser design in 1975, when he presented his theory of reflection phase grating diffusers [30],[25]. Schroeder diffusers offered a key advantage in that their performance could easily be predicted, and they are still considered amongst some of the the most effective diffuser designs used today. Schroeder diffusers are typically more efficient at promoting diffusion than many other protruding geometries such as rectangular, cubic, triangular, polycylindrical and spherical shapes [11].

Recent advancements in computing power and the requirement for diffusers to fit with modern architecture and interior design have led to surface profiles derived from numerical optimisation. Numerically optimised diffusers may contain a hybrid of absorption and reflecting components, and surface profiles containing curved and square edge components [7]. The pseudo-random profile of the diffusers is optimised through computer modelling, and results may apply only to that particular size or application. Unlike Schroeder diffusers which have known and repeatable diffusion characteristics, numerically optimised diffusers are designed for high performance only at the conditions modelled during optimisation [6].

Diffusers with a surface profile described by two dimensions, such as an infinite cylinder, are labelled one dimensional diffusers, whereas diffusers with a three dimensional

profile such as a sphere, are labelled two dimensional diffusers. Typically, one dimensional diffusers scatter a sound wave two dimensions, and two dimensional diffusers scatter a sound wave in three dimensions. The main focus of this work is one dimensional Quadratic Residue Diffusers, though a background introduction will be given to other common diffuser types.

2.4.2 Curved and cylindrical surfaces

A cylinder is an efficient two-dimensional diffuser [7]. With a simple design and shape commonly found in architecture, the ability to model its behaviour is helpful to acoustic space design. While sufficiently large cylinders have high quality diffuse properties, their application as an acoustic treatment is limited by their size, as well as lack of repeatability; a row of half cylinders along a wall do not have the same high standard of diffuse properties [7]. Diffraction from singular cylinders and spheres was modelled analytically by Weiner [31], and the diffraction from a set of half cylinders modelled using the Boundary Element Method by Cox & D'Antonio [7]. The ability to analytically solve diffusion from a cylinder and sphere make them ideal test cases for BEM model validation (see Chapter 5.2).

2.4.3 Schroeder diffusers

In two dimensions, Schroeder phase grating diffusers consist of wells of even width and varying depth separated by thin panels. Different mathematical patterns govern the depth of successive wells. Schroeder predicted that high levels of diffusion could be obtained through a surface profile of two different heights following the Maximum Length Sequence (see Chapter 2.4.3.1) [25]. On top of this, Schroeder predicted that a phase delay, or temporal diffusion, could be obtained when the well depths follow certain patterns such as the Quadratic Residue sequence (see Chapter 2.4.3.2) [26] and the Prime-Root sequence (see Chapter 2.4.3.3) [11].

Schroeder diffusers are commonly used in repeating periods, where the diffusion effects from a single period are enhanced by repetition. A period consists of N wells of width w, separated by a thin panel of width $w_{_P}$. The total width of a well and panel is represented by w_T, and consequently the period width is written as Nw_T, shown in Figure 2.4.3a. One of the principles underpinning Schroeder diffusers is that the periodic nature of the patterns governing the surface profiles causes sound pressure lobes in

the polar diffusion patterns, an example of which is shown in Figure 2.4.1. These lobes are caused by the interference of delayed reflections from varying well depths, and give Schroeder diffusers their high diffusion properties. The number and strength of these diffusion lobes is governed by many factors including frequency and diffuser dimensions.

A design principle behind Schroeder's theory of phase grating diffusers is that longitudinal wave propagation within the wells dominates transverse waves. From this, the upper frequency limit to the applicability of this theory can be stated as

$$\lambda_{min} = 2w\,, \tag{2.4}$$

where λ_{min} is the minimum wavelength corresponding to the maximum frequency. Beyond this frequency, Schroeder diffusers may continue to display diffusive properties but they may be less effective and consistent. The diffusion performance of QRDs at frequencies above this point is investigated in Part III of this work.

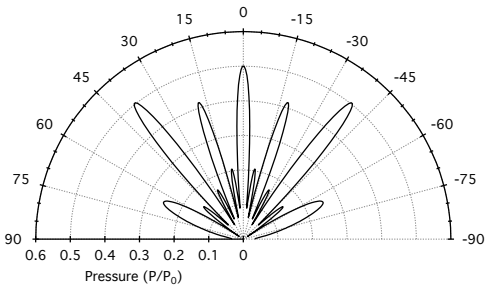

Figure 2.4.1: Example of energy lobe diffraction pattern from $N = 7$ QRD at 4 times f_0. $P = 3$, $Nw_T = 0.56$ m, $f_0 = 500$ Hz.

2.4.3.1 Maximum Length Sequence diffusers

Maximum Length Sequence (MLS) diffusers were the first type of reflection phase grating diffuser suggested by Schroeder in 1975 [25], and are the simplest form of Schroeder diffuser. MLS diffusers are a one dimensional diffuser with even width sections of two different heights. The height of each well is governed by the Maximum Length Sequence, a pseudo-random binary sequence derived using maximal linear feedback shift registers. Figure 2.4.2 shows an example of a MLS diffuser sequence. MLS diffusers are rarely used because alternative Schroeder diffusers such as QRDs and PRDs offer superior diffusion characteristics.

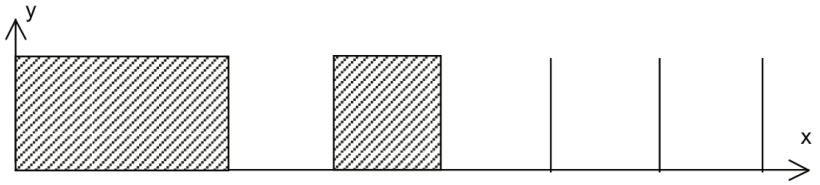

Figure 2.4.2: Cross section of N=7 MLS diffuser. From Cox & D'Antonio p.296 [7].

2.4.3.2 Quadratic Residue Diffusers

The most popular Schroeder diffuser is the Quadratic Residue Diffuser (QRD). Similar to MLS diffusers, QRDs consist of evenly spaced wells divided by thin panels. Well depths are governed by the Quadratic Residue Sequence first studied by Gauss and Legendre [26]. The n^{th} term in the sequence, s_n, is defined as

$$s_n = n^2 \,\text{modulo}(N)\,, \tag{2.5}$$

where $n = 0, 1, 2 \ldots (N-1)$, and modulo(N) represents the least non-negative remainder when divided by a multiple of N. The value N is restricted to prime numbers, and also represents the number of terms in each repeating sequence. In this way, the Quadratic Residue Sequence is restricted to sequence lengths of 5, 7, 11... [25]. An example $N = 7$ quadratic residue sequence is calculated in Table 2.4.1, and a corresponding QRD is pictured in Figure 2.4.3.

Table 2.4.1: Quadratic Residue Sequence calculation example for $N = 7$

$\boldsymbol{n}$	**0**	**1**	**2**	**3**	**4**	**5**	**6**
$\boldsymbol{n^2}$	0	1	4	9	16	25	36
$\boldsymbol{n^2}$ **modulo(7)**	0	1	4	2	2	4	1

Schroeder used a Fourier transformation and representation of a QRD as a plane surface with varying complex surface impedance (corresponding to well depths) to show that QRD diffusion patterns at design frequencies display lobes of even energy in different angular directions [26]. The design frequency of a QRD, f_0, is the lowest frequency at which even energy diffusion lobes can be expected [26]. The design and determines the

scaling factor applied to all terms in the quadratic residue sequence when applied to a QRD. Even energy lobes can be predicted at multiples of this design frequency. However, between these frequencies QRDs can still display high diffusion properties (see Part III). The depth of well n, d_n, in a quadratic residue diffuser for a design frequency of f_0 and prime number N are determined from the equation

$$d_n = \frac{c}{2Nf_0} s_n \,, \tag{2.6}$$

where c is the speed of sound in air [25].

Another limiting factor of QRDs is the period width Nw_T. While even energy lobes can be expected at the design frequency f_0, if the period width is too small only one energy lobe is present in the specular reflection direction, and the diffuser displays poor diffusion characteristics [7]. In Part III of this investigation, this effect is reproduced and the relationship between period width and lowest frequency of significant diffusion is investigated.

A feature of quadratic residue diffusers, and indeed of any Schroeder diffuser is their ability to act as a plane surface at frequencies where all well depths are a multiple of half the wavelength. The first frequency at which this will occur is termed the critical frequency f_c, and Schroeder diffusers can be expected to display very poor diffusion characteristics around this frequency [26]. For quadratic residue diffusers, the critical

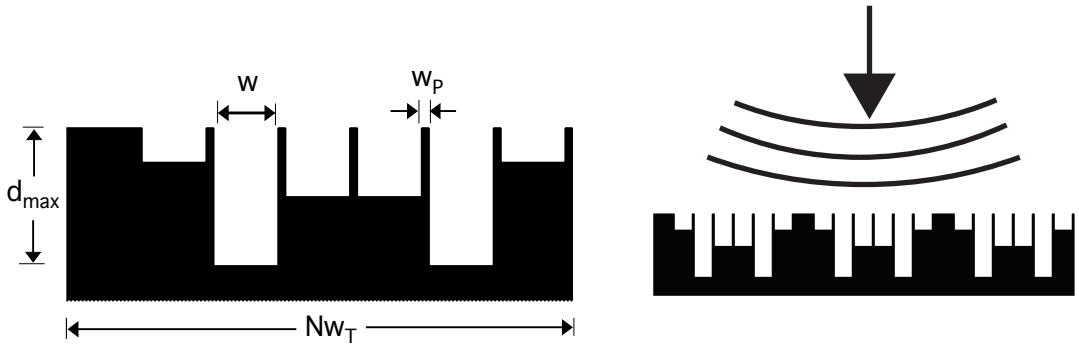

(a) $P = 1$ (b) $P = 3$

Figure 2.4.3: Example of $N = 7$ QRD in single and repeating periods.

frequency occurs where the first well depth is equal to half the critical frequency wavelength λ_c [7]. Using the relationship

$$\lambda_c/2 = d_1\,,$$

and combining with Equation (2.6), f_c can be described in terms of the design frequency as

$$f_c = N f_0\,. \tag{2.7}$$

It can be seen from (2.7) that QRDs based on sequences with larger values of N will have a larger range between the design frequency and the critical frequency. It is suggested by Cox & D'Antonio that the critical frequency should not be located within the desired diffusion bandwidth. [7]

Theoretically, the width of the well diving panels should be the minimum possible. It is important however that they are thick enough to act as a rigid surface. An advantage of modelling QRDs without using the thin panel method (see Chapter 2.5.2.1) is that the effect of varying well divider panel widths on diffusion performance can be modelled, and this is also investigated in Part III of this work.

The quadratic residue sequence as described by Equation (2.5) is naturally asymmetrical. The first term s_0 is 0, and the last term s_{N-1} is 1, independent of N. For reasons of cost and desired symmetry, QRDs are often manufactured as a symmetrical sequence, with the first well width halved, and an additional well of width $w/2$ and depth 0 added at the end of the sequence. For installations of multiple QRD periods, internal connections of well depth 0 have width w, whereas the first and last wells of the installation will have width $w/2$.

The absorption of QRD panels is of interest to those designing acoustically critical spaces. In many environments minimal absorption is desired, and QRDs are designed accordingly. Three main variables affect the absorption of QRDs: the relative width and depth of wells; the build material; and the build quality. QRDs with long thin panels can experience higher levels of absorption due to interaction of pressure waves and fluid boundary layers along panels [7]. Wood is commonly used as a build material due to its efficient reflective properties. Other materials sometimes used include glass, moulded

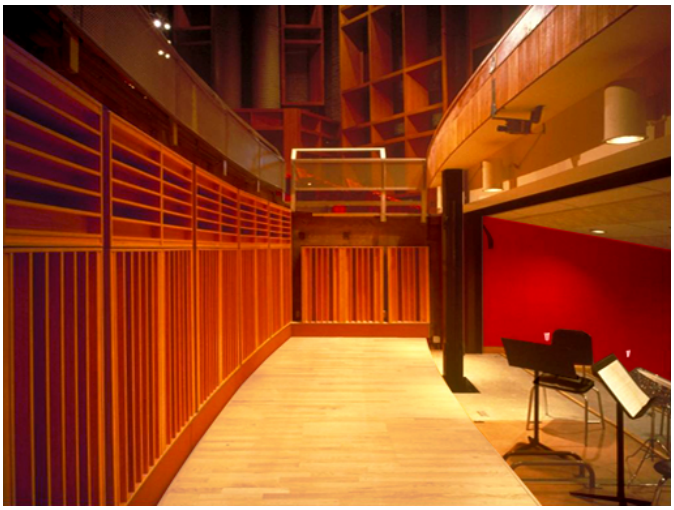

Figure 2.4.4: $N = 7$ QRD array of multiple repeating periods. From RPG Diffusor Systems [10].

plastic, expanded polystyrene and sheet metal [7].

The build quality can have a large effect on the absorption properties of a QRD. Fujiwara & T. Miyajima [15] recorded absorption coefficients for QRDs between 0.3 and 1, in particular at frequencies below the design frequency. They later investigated these high values of absorption and found that it was predominantly due to poor build quality and bonding of the QRDs tested [14]. Data from commercially available QRDs list absorption coefficients between 0.2 and 0.3 [16].

2.4.3.3 Primitive Root Diffusers

Primitive Root Diffusers (PRDs) are very similar in design to QRDs in that they consist of a series of wells of similar widths and varying depths. Well depths follow the Primitive Root Sequence, defined as

$$s_n = r^n \,\text{modulo}(N) \tag{2.8}$$

for $n = 1, 2, \ldots N$. s_n is the n^{th} term in the sequence, N is a chosen prime number and r is the corresponding primitive root of N. The sequence has $N - 1$ terms, and the primitive root r of any given prime number is one that all s_n in the sequence are unique. Primitive root values for their respective prime numbers can be found through trial and error or are tabulated in Reference [12]. An example calculation of a Primitive Root Sequence is included in Table 2.4.2 for $N = 7$ and the corresponding primitive root $r = 3$.

Table 2.4.2: Primitive root Sequence calculation example for $N = 7$, $r = 3$.

Sequence number	**1**	**2**	**3**	**4**	**5**	**6**
$\boldsymbol{r^n}$	3	9	27	81	243	729
$\boldsymbol{r^n}$ **modulo**$(\boldsymbol{N})$	3	2	6	4	5	1

PRDs are designed to display the same even energy lobes as QRDs, as well as have reduced diffusion in the specular reflection direction. It is found that in the order of 20 to 30 wells are needed to produce a noticeable reduction of reflected energy in the specular reflection direction [7], and the frequency range in which it is occurs is minimal [13]. PRDs generally have poorer diffusion characteristics [7] and are also inherently asymmetric, which is perhaps why QRDs are largely more popular than PRDs.

2.4.4 State-of-the-art on QRD design

2.4.4.1 Fractal diffusers

In an effort to increase the optimum diffusion frequency range for QRDs, panels at the bottom of wells can be replaced by a smaller QRD with period width $(Nw_{_T})_{\text{frac}}$ equal to the larger QRD well width w. This is an effective method for increasing diffusion at frequencies for which the larger QRD would otherwise become less effective due to transverse wave propagation within wells. Additionally, repeating periods of QRDs can be installed with a varying datum following the quadratic residue sequence, which assists in increased low frequency diffusion, as well as reducing the effect of undesirable strong lobe concentrations [7]. An example of a commercially available fractal is the QRD Diffractal, developed by D'Antonio & Konnert [9]. The Diffractal incorporates three levels of fractals within its design and produces high diffusion performance across a wider bandwidth than standard QRDs. Fractals were shown to be an effective way at extending the diffusion bandwidth during this study (see Chapter 7.2).

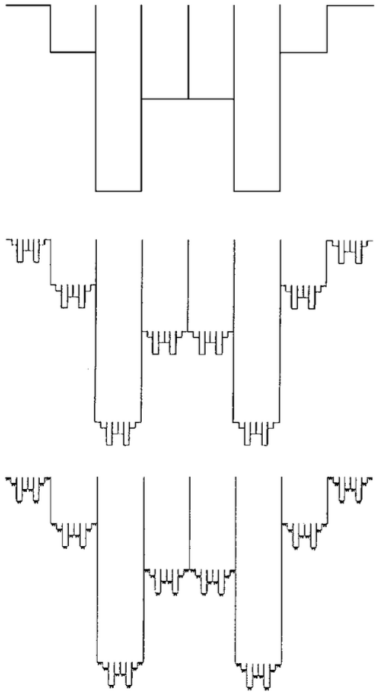

Figure 2.4.5: An $N = 7$ QRD design with two levels of fractals. (Everest & Pohlmann p. 269 [11]).

2.4.4.2 Modulated QRDs

The quadratic residue sequence can be modulated so that the n^{th} term, s_n, is described as

$$s_n = (n^2 + k) \,\text{modulo}(N)\,, \tag{2.9}$$

where k is an integer constant. This introduces a constant phase shift to all terms in the sequence. Table 2.4.3 shows the tabulated series for a regular Quadratic Residue Sequence and modulated Quadratic Residue Sequence. In this example, the maximum term number of the regular sequence is 12, and the maximum term for the phase shifted sequence is 8. It follows from Equation (2.6) that the maximum depth of a QRD following the phase shifted sequence will be 2/3 that of the regular sequence for a similar design frequency. This can be useful in lowering the design frequency when depth constraints are present, or in reducing losses in QRDs with narrow wells.

Table 2.4.3: Example of regular and phase shifted $N = 13$ Quadratic Residue Sequence with value $k = 4$.

$\boldsymbol{n}$	0	1	2	3	4	5	6	7	8	9	10	11	12
$\boldsymbol{n^2}\,\textbf{modulo}(\boldsymbol{N})$	0	1	4	9	3	12	10	10	12	3	9	4	1
$(\boldsymbol{n^2+4})\,\textbf{modulo}(\boldsymbol{N})$	4	5	8	0	7	3	1	1	3	7	0	8	5

2.4.4.3 Three-dimensional Schroeder Diffusers

The application of the Quadratic Residue Sequence in diffuser design is not limited to one-dimensional diffusers. The sequence can be effectively layered on top of itself in two different dimensions to produce a surface profile consisting of square wells of different depths [11]. Two-dimensional Schroeder diffusers are capable of efficient three-dimensional diffusion often utilised to provide improved diffusion from ceiling reflections [26].

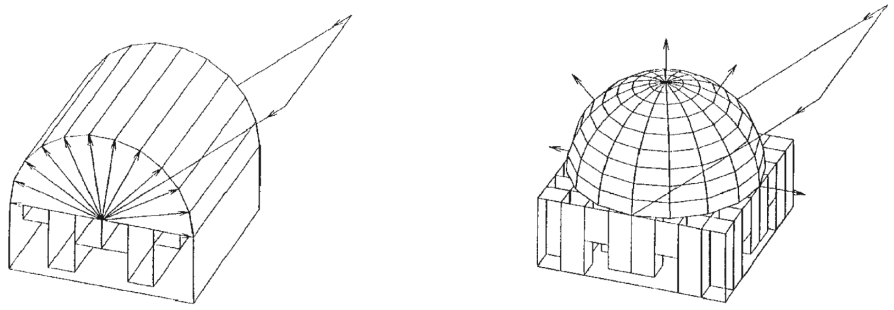

(a) One-dimensional QRD

(b) Two-dimensional QRD

Figure 2.4.6: QRD and diffusion pattern for one-dimensional and two-dimensional QRDs. Adapted from Everest & Pohlmann p. 271 [11].

2.5 BEM

The Boundary Element Method (BEM) is a numerical method for solving the partial differential equations that govern physical systems. It is used in the fields of stress analysis, potential flow and acoustics [17]. In acoustic applications such as this work, the BEM can be used to solve the Helmholtz equation for interactions between an incident acoustic field and one or more surfaces within the field, and can be used to model acoustic fields in both two and three dimensions. The BEM replaces the partial differential equation governing the domain solution with an equation governing the solution at the domain boundary, and through surface discretisation and knowledge of the surface boundary conditions, calculates a solution for the boundary acoustic potential (see Chapter 4.2). From this solution the acoustic potential at any chosen point within the domain can be calculated individually. The large advantage therefore with the BEM as compared to Finite Element Analysis is a surface only requires discretisation, and a solution at any point within any sized domain can be calculated without adverse implications for computational time and storage requirements. Finite Element Analysis requires a whole

domain of interest to be discretised, which reduces its practical application for large domains or high frequencies that require small elements. The theory behind an acoustic diffusion implementation of the BEM is included in Chapter 4.

2.5.1 Conditions and Limitations

2.5.1.1 Continuous surface geometry

Using Green's Second Identity (Eq. 4.5), the BEM computes a closed surface integral around the object within the acoustic field [17]. Tests for this study encountered errors when attempts were made to model an open surface with the BEM. Using the regular BEM, thin panels must be represented with a finite width, and errors can also be encountered when thin panels are modelled without appropriately small elements (see Chapter 5.2.5.1). A method called the thin panel solution exists for the representation of thin panels as having infinitely small width, while still satisfying Greens Second Identity, and avoids thin panel errors (see Chapter 2.5.2.1).

2.5.1.2 Non-unique solutions

When solving the simultaneous equations for surface pressures as part of the BEM, it is possible to get non-unique solutions at certain frequencies which correspond to the eigensolutions of the interior of the geometry being modelled. [7][17]. One of multiple solutions to this problem is the CHIEF method. The CHIEF method adds an additional constraint to the solution by requiring the pressure at one or more receivers within the geometry surface to equal 0, which is satisfied only for correct solutions. The exception to this is that internal receivers may be unknowingly placed at nodes of the incorrect internal eigensolution where the pressure is 0. Seybert & Rengarajan [27] showed it is generally a very effective method at avoiding the problem of non-unique BEM solutions. Cox & D'Antonio however state that it is rarely encountered when modelling acoustic diffusers.

A simple but less efficient method of checking whether a BEM solution is a result of non-unique solutions error was developed in the BEM code during this work, and is discussed in Chapter 5.1.5.

2.5.2 State-of-the-art on BEM modelling

2.5.2.1 Thin panel solution to BEM modelling

When using the BEM to model geometry that contains thin panels or surfaces, errors are sometimes encountered due to the proximity of front and back elements [7]. Terai [29] published a solution to this in which a thin panel is represented as having infinitesimal thickness and modelled as a surface instead of a closed boundary, and results in a solution for pressure on the front and back of these surface elements. Wu [32] took this thin panel solution further, and developed a method to integrate it with the regular BEM method so that a combination of the regular BEM and thin panel solution BEM can be used together. While offering a solution to the errors caused by thin panels in geometry such as QRDs, it also reduces the number of elements needed and decreases computation times.

The need for the thin panel solution has arguably decreased as computation power has increased. In 1994, Cox & Lam [8] noted a running time of 10 hours for a BEM model of a QRD consisting of 768 elements at one frequency. Element sizes small enough to model thin panels without errors were not possible, so the alternative to the thin panel solution was a 'box model' with varying complex surface impedance to represent the phase delay of QRD wells, thereby neglecting the effects of any non-longitudinal wave propagation within wells. The thin panel solution therefore provided a strong advantage over other methods at the time. With the increase in computer storage and computing power today, as well as methods to increase efficiency of meshing and computation (see Chapter 5.2) BEM models are much faster.

The BEM program developed in this work takes approximately 13 seconds for a similar QRD model of 768 elements (see Chapter 5.2.6). The element length needed to avoid thin panel errors was also investigated in Chapter 5.2.5.1, and it is shown that element sizes needed to avoid thin panel errors are achievable with reasonable running times. Using this, the BEM model accurately represents a QRD including thin panel thickness, which can effect results, particularly at high frequencies.

2.5.2.2 Three dimensional modelling with the BEM

While the focus of this study is the application of the BEM in two-dimensions, it is also an effective method of modelling in three dimensions. Three-dimensional modelling requires particular attention to the geometry discretisation, where elements must be represented by small flat panels, instead of straight lines for the two-dimensional case, and this is where human error will most likely occur [7].

The BEM in three-dimensions is useful tool to model surface profiles that vary in three dimensions, such as a sphere or two-dimensional QRD. However, Cox & Lam [8] showed the two-dimensional BEM is accurate in predicting the diffusion patterns of one-dimensional diffusers, and the additional computation time necessary for three-dimensional modelling is not necessary.

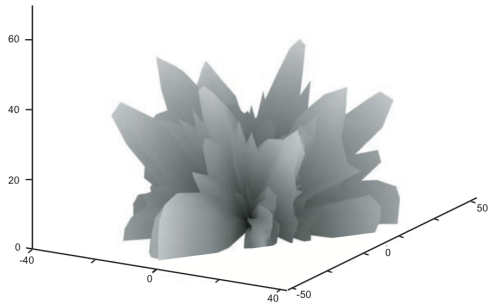

Figure 2.5.1: A two-dimensional diffuser modelled using a three-dimensional BEM. From Cox & D'Antonio p. 320 [7].

Part II

BEM Code Development and Optimisation

Chapter 3

MATLAB BEM Overview

Part I of this work is the further development and optimisation of a MATLAB implementation of the BEM. The theory used in gaining a solution using the BEM is derived in detail (Chapter 4). Significant changes and developments to the code are documented (Chapter 5), including methods to increase the solution speed and accuracy. The BEM code is then tested in comparison to an analytical solution (Chapter 5.2.2), published results (Chapter 5.2.3) and the original BEM code (Chapter 5.2.6). A detailed accuracy study is also conducted with reference to model geometry, frequency and element size, from which recommendations are made for the appropriate use of the code when modelling Schroeder diffusers (Chapter 5.2.5).

A brief description of executing the BEM code, and major MATLAB functions within the code is given (Chapter 3.2). A tabulated breakdown of the program steps used in the BEM is described in Appendix B.1. A flowchart shows the MATLAB functions used in the calculation of different variables, including acoustic field types and frequency bands (Chapter 3.2.1).

3.1 Acknowledgements

This work is a continuation of the works of Luca Rocchi [23] and Nick Smith [28], who in 2013 implemented the BEM into a MATLAB function and validated its accuracy against both published literature and Finite Element Analysis models. Some sections of code are completely re-written while others are largely untouched. A guide to the author of sections is given in the individual function comments. Credit should be given to Rocchi and Smith for the initial implementation and ideas used to solve the BEM problem.

3.2 Executing the BEM code

The BEM code can be executed from the MATLAB function `run_BEM` . All test parameters can be assigned values within this function, and it includes geometry creation functions for most common QRD designs and modifications. `run_BEM` can be modified to return output results as necessary.

`run_BEM` executes multiple subroutines as part of obtaining a solution. A summary of major subroutines is included in Table 3.2.1. *(ext.)* indicates multiple version of the code exist with different names for different input parameters, such as frequency band averages and incident acoustic source types. Many other subroutines are involved in geometry creation and minor calculations, and are described in the relevant function comments.

Table 3.2.1: BEM code subroutines

Subroutine	**Description**
`BEM`	The governing function that computes the BEM solution. Executes the relevant functions for calculations based on input parameters, shown in Figure 3.2.1.
`diff_disc`	Discretises the geometry into elements from a set of corner points.
`num_gauss_points`	Calculates the number of gauss points required for numerical integration of each pair of elements.
`b_cond`*(ext.)*	Computes the boundary condition. Multiple functions are used for different test parameters.
`coeff_matrix_creation_ON`*(ext.)*	Computes the matricies [M] and [L] for surface elements.
`m_eq_1`*(ext.)*	Solves the matrix equation for surface element pressures
`coeff_matrix_OFF`*(ext.)*	Computes the matricies [M] and [L] for reciever pressures
`m_eq_2`*(ext.)*	Solves the matrix equation for receiver pressures
`diff_coeff_calculator`*(ext.)*	Computes diffusion coefficeints form diffusion data

3.2.1 BEM code flowchart

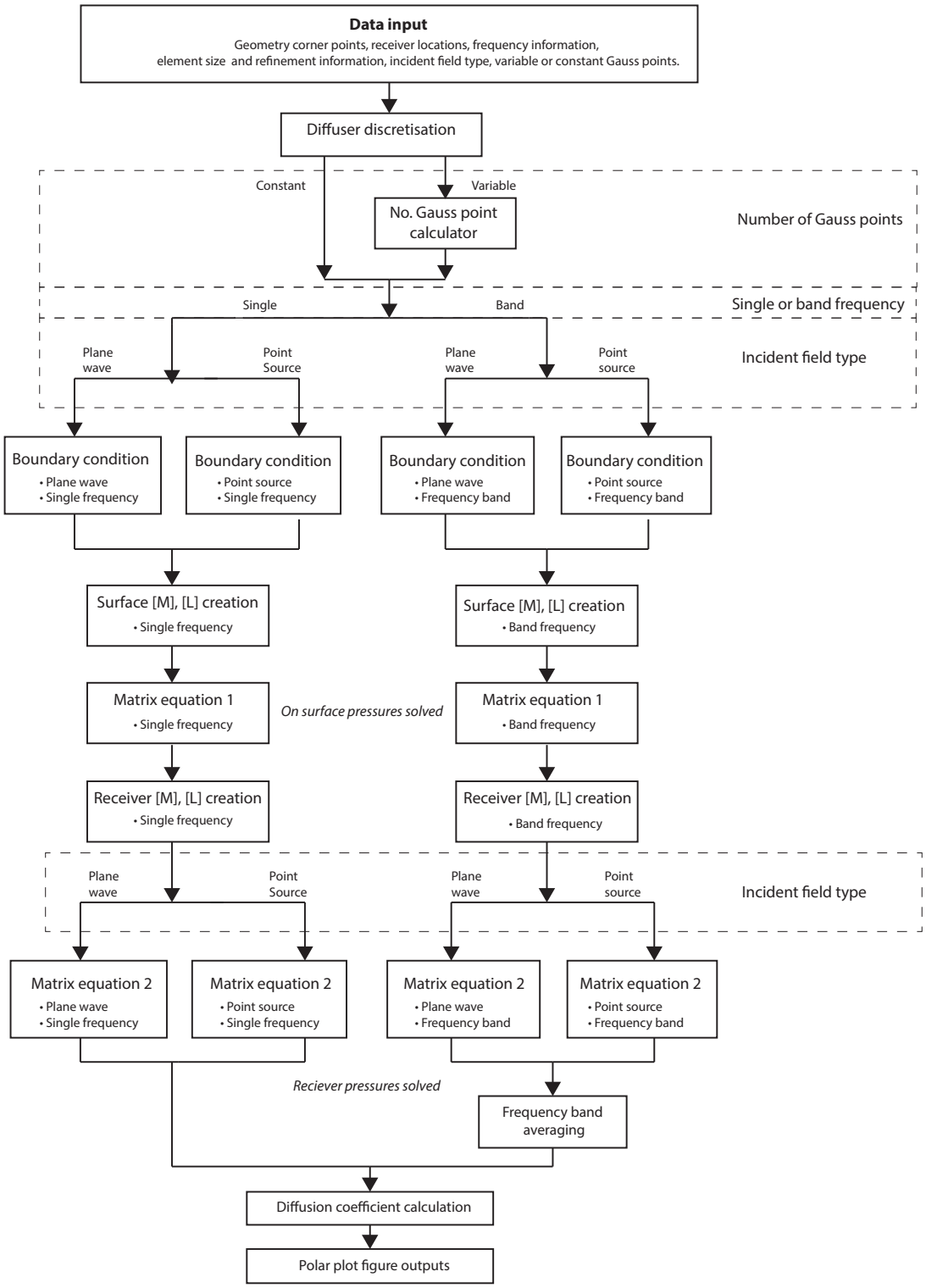

Figure 3.2.1: Flowchart of current BEM code.

Chapter 4

BEM Theory

4.1 BEM assumptions

During this implementation of the BEM for acoustic modelling, the following assumptions are made:

1. The surface is rigid and acts as a perfect reflector, with no sound absorption or transmission through the geometry medium. It is possible to apply a surface impedance to simulate absorption. However, the effectiveness of this for Schroeder diffusers may be questioned, in particular at lower frequencies, as research shows factors such as build quality and panel bonding techniques can affect absorption as much as the build material (see Chapter 2.4.3.2).

2. The acoustic field is a combination of the incident field and modelled surface reflections only. The domain is considered infinite or as having a boundary with an absorption coefficient $\alpha = 1$.

3. The domain is an isotropic homogeneous fluid. Pressure wave energy losses due to viscous effects are negligible, and may be ignored.

The above assumptions are reasonable for acoustic modelling of diffuser geometries in room temperature air within the approximate range of 100 - 7000 Hz. Assumption 1 holds well for most rigid diffusers, particularly as most commercial products are designed for minimal absorption (see Chapter 2.4.3.2). Assumption 2 is a simplification made for the purpose of modelling and performance characterisation. While incident waves may be dominant for many diffuser applications, the sound field will consist of an incident wave together with reflections from other surfaces including walls and floors. A transient wave can accurately replicate an infinite boundary within the time taken for first order reflections from other surfaces to reach a receiver, as done by Cox & D'Antonio [7]. Assumption 3 may not be applicable when modelling with higher frequencies and large

distances, or in media with high viscosity, where attenuation from viscous energy losses must be taken into account.

4.2 Wave theory

A sound field of periodic waves can be represented by a potential function $\phi(\boldsymbol{p})$, where $\boldsymbol{p}$ is an arbitrary point within the domain[1], and $\phi(\boldsymbol{p})$ satisfies the Helmholtz equation

$$\nabla^2\phi + k^2\phi = 0\,, \tag{4.1}$$

where k is the wavenumber, representing the number of cycles per unit distance $k = \frac{2\pi f}{\upsilon}$, f represents frequency (Hz), and υ represents the wave phase velocity (m/s). The wave potential function $\phi(\boldsymbol{p})$ describes the pressure P at any point $\boldsymbol{p}$, as:

$$P = -\rho\frac{\partial\phi}{\partial t} = i\rho\omega\phi\,, \tag{4.2}$$

$$\boldsymbol{V} = \nabla\phi\,. \tag{4.3}$$

Both P and ϕ are assumed to be sinusoidal, and are represented as complex variables, in which absolute value represents magnitude and argument represents relative phase. For an open sound field, we can write the sound field as the superposition of the incident and diffracted sound fields

$$\phi_{\text{total}} = \phi_{\text{incident}} + \phi_{\text{diffracted}}\,. \tag{4.4}$$

From here onwards, the subscripts T, I and D represent total, incident and diffracted respectively. From (Eq. 4.3) we can extend this to superposition of the incident and diffracted acoustic wave velocity

$$\boldsymbol{V}_T = \boldsymbol{V}_I + \boldsymbol{V}_D\,. \tag{4.5}$$

4.3 Incident sound field

When modelling diffusion in two dimensions, there are two obvious choices for an incident sound field: that of a incident plane wave, and that of a point source located at some

[1]During this work, bold denotes a vector.

point in the external domain. For the purpose of a BEM analysis, the incident sound field must be modelled at a snapshot in time, in which time is constant and pressure is a function of position only. For the case of an incident plane wave, ϕ takes the form

$$\phi = \phi_o e^{-ikx}\,, \tag{4.6}$$

where

$$\frac{\partial \phi}{\partial x} = -ik\phi_0 e^{ikx}\,,$$

$$\frac{\partial \phi}{\partial y} = \frac{\partial \phi}{\partial z} = 0\,.$$

A point source incident sound field can be represented by the Hankel function as

$$\phi = H_0^{(1)}(kr)\,, \tag{4.7}$$

and from Chapter 4.7,

$$\frac{d}{dr}H_0^{(1)}(kr) = -kH_1^{(1)}(kr)\,,$$

where r is the magnitude of the vector between the point source and receiver. The Hankel function is undefined at a value of $kr = 0$ (see Chapter 4.7). However, it can be scaled by a constant as needed to interpret results.

4.4 Rigid body boundary condition

The implementation of the Boundary Element Method requires knowledge of the boundary conditions along a surface. During this investigation, it is assumed that the surface is perfect reflector, expressed mathematically as $\boldsymbol{V}_T \cdot \hat{\boldsymbol{n}} = 0$, where $\hat{\boldsymbol{n}}$ is the unit outward normal vector from any point on the boundary. Using this result we can reduce equation (Eq. 4.5) to

$$\boldsymbol{V}_D \cdot \hat{\boldsymbol{n}} = -\boldsymbol{V}_I \cdot \hat{\boldsymbol{n}}\,,$$

and combined with (Eq. 4.3), this becomes

$$\frac{\partial \phi_D}{\partial \hat{\boldsymbol{n}}} = -\boldsymbol{V}_I \cdot \hat{\boldsymbol{n}}\,. \tag{4.8}$$

For simplicity, the subscript D for ϕ will be assumed

4.5 Green's second identity

Green's Second Identity, derived from the divergence theorem, can be written as

$$\oiint \left(\phi(\boldsymbol{q}) \frac{\partial G(\boldsymbol{p}, \boldsymbol{q})}{\partial n_q} - G(\boldsymbol{p}, \boldsymbol{q}) \frac{\partial \phi}{\partial n_q} \right) \mathrm{d}S_q = -C\phi(\boldsymbol{p}) \,, \tag{4.9}$$

where $G(\boldsymbol{p}, \boldsymbol{q})$ represents the effect of a unit source at $\boldsymbol{q}$ on a point $\boldsymbol{p}$. From the definition of G given in (Eq. B.10), the coefficient C has values of:

- 0 for points not within the domain;
- 0.5 for points that lie on the boundary; and
- 1 for points within the boundary.

Substituting in the Rigid Body Boundary Condition (Eq. 4.8) gives

$$\oiint \left(\phi(\boldsymbol{q}) \frac{\partial G(\boldsymbol{p}, \boldsymbol{q})}{\partial n_q} - (-\boldsymbol{V}_I \cdot \hat{n_q}) G(\boldsymbol{p}, \boldsymbol{q}) \right) \mathrm{d}S_q = -C\phi(\boldsymbol{p}) \,, \tag{4.10}$$

This is an important result, and is the basis of the Boundary Element method. It allows the sound potential at any point on the surface $\phi(\boldsymbol{p})$ to be written in terms of the surface geometry and the incident sound field. A derivation of Green's second identity from the divergence theorem is shown in Appendix B.2.

4.6 Discretisation of the boundary

To apply the Boundary Element Method to any arbitrary surface, it must first be discretised into a number of small segments, with the assumption that ϕ is constant across that section.

This assumption enables us to describe Green's Second Identity (Eq. 4.9) for any element ϕ_i in a discretised form as

$$C\phi_i = \sum_{j=1}^{n} \left(\phi_j \int_{q_{j-1}}^{q_j} (\nabla G \cdot \hat{\boldsymbol{n}}_j) \, \mathrm{d}S + (\boldsymbol{V} \cdot \hat{\boldsymbol{n}}_j) \int_{q_{j-1}}^{q_j} G \, \mathrm{d}S \right) ,$$

or using simplified notation

$$C\phi_i = \sum_{j=1}^{n} (\phi_j \mathrm{M}_{ij} + (\boldsymbol{V} \cdot \hat{\boldsymbol{n}}_j)\mathrm{L}_{ij}) \ , \tag{4.11}$$

where

$$\mathrm{M}_{ij} = \int_{q_{j-1}}^{q_j} \nabla G(p_i, q_j) \cdot \hat{\boldsymbol{n}} \, \mathrm{d}S \, , \tag{4.12}$$

$$\mathrm{L}_{ij} = \int_{q_{j-1}}^{q_j} G(p_i, q_j) \, \mathrm{d}S \, . \tag{4.13}$$

Substituting in $C = -\frac{1}{2}$, (Eq. 4.11) can be written in terms of a vector of all surface potential values $\{\phi\}$ as

$$-\frac{1}{2}[I]\{\phi\} = [\mathrm{M}]\{\phi\} + [\mathrm{L}]\{\boldsymbol{V}_I \cdot \hat{\boldsymbol{n}}\} \tag{4.14}$$

and combining the two $\{\phi\}$ terms,

$$-[\mathrm{L}]\{\boldsymbol{V}_I \cdot \hat{\boldsymbol{n}}\} = \left([\mathrm{M}] + \frac{1}{2}[I]\right)\{\phi\} \, . \tag{4.15}$$

(Eq. 4.15) can be used to solve for the vector of surface potential values $\{\phi_{\text{surf}}\}$. Off surface potential can be solved through substituting this into the right hand side of (Eq. 4.14), and replacing the left hand side with $\{\phi_{\text{off-surf}}\}$.

4.7 The Hankel functions

So far, the sound field intensity at each point on a surface has been described using a function that relates the effect of a unit source at point $\boldsymbol{q}$ has on point $\boldsymbol{p}$; $G(\boldsymbol{p}, \boldsymbol{q})$. This function must satisfy the Helmholtz equation (Eq. 4.1). For two-dimensional waves, this function can be represented by the Hankel functions of the first kind and order zero as published by Abramowitz and Stegun [4]:

$$H_\nu^{(1)}(z) = J_\nu(z) + iY_\nu(z) \, , \tag{4.16}$$

and

$$G(\boldsymbol{p}, \boldsymbol{q}) = \alpha H_0^{(1)}(kr)$$

where $J_\nu(z)$ and Y_ν the Bessel functions of the first and second kind respectively, both of order ν, r is the magnitude of the distance between $\boldsymbol{p}$ and $\boldsymbol{q}$, and α is a constant. The Hankel functions are chosen because they satisfy the Helmholtz equation in cylindrical coordinates.

To calculate the coefficient α, we recall that in the derivation of Green's Second Theorem (Appex. B.2), the function $G(\boldsymbol{p}, \boldsymbol{q})$ was scaled so that

$$\frac{\partial G}{\partial r} = \frac{1}{2\pi r} \text{ as } r \to 0\,. \tag{4.17}$$

From Abramowitz and Stegun [4],

$$-iH_0^{(1)}(z) \sim \frac{2}{\pi}\ln(z) \text{ as } z \to 0\,,$$

hence

$$\frac{d}{dz}H_0^{(1)}(z) \sim \frac{2i}{\pi z} \text{ as } z \to 0\,. \tag{4.18}$$

Combining (Eq. 4.17) and (Eq. 4.18) to solve for α,

$$\frac{dG(kr)}{dr} = k\frac{dG(kr)}{d(kr)} \to kC\frac{2i}{\pi kr} = \frac{1}{2\pi r} \text{ as } r \to 0\,,$$

and

$$\alpha = \frac{i}{4}\,. \tag{4.19}$$

Abramowitz and Stegun [4](Ch. 9.1.28) also state the relationship

$$Y_o'(z) = -Y_1(z)\,,\; J_0'(z) = -J_1(z) \text{ as } z \to 0$$

and from (Eq. 4.16) it follows that

$$\frac{d}{d(kr)}H_0^{(1)}(kr) = -H_1^{(1)}(kr)\,, \tag{4.20}$$

and

$$\frac{d}{dr}H_0^{(1)}(kr) = -kH_1^{(1)}(kr)\,. \tag{4.21}$$

The results from (Eq. 4.19) and (Eq. 4.21) combine to give the two appropriately scaled

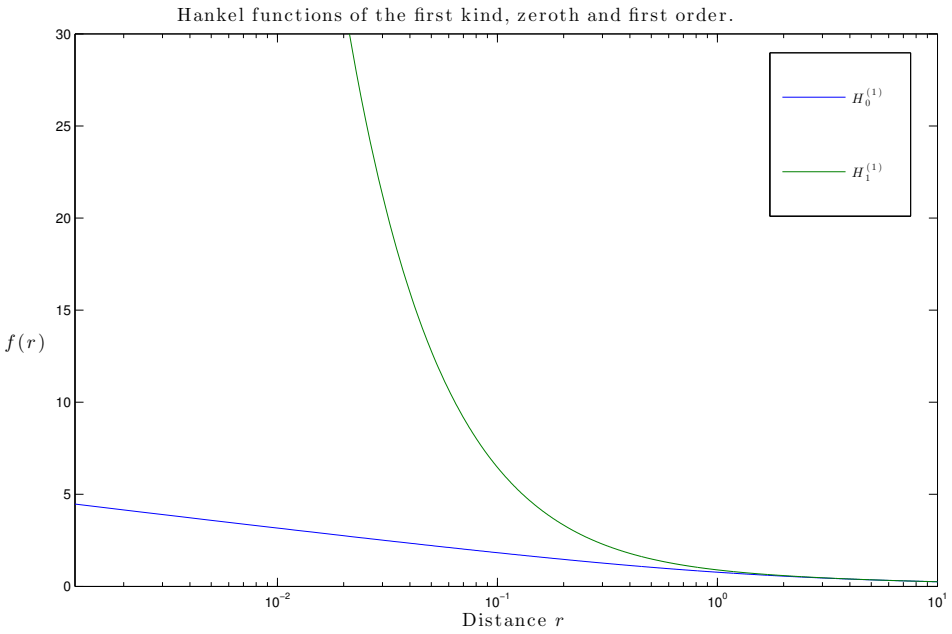

Figure 4.7.1: Absolute value of Hankel functions of constant k and increasing r.

equations used to model the effect of a unit source on a point:

$$G(\boldsymbol{p},\boldsymbol{q}) = \frac{i}{4}H_0^{(1)}(kr)\,, \tag{4.22}$$

$$\frac{\partial G(\boldsymbol{p},\boldsymbol{q})}{\partial \hat{\boldsymbol{n}}} = -\frac{ik}{4}H_1^{(1)}(kr)\,. \tag{4.23}$$

For any given wavenumber, these functions decrease with an increase in r as shown in Figure 4.7.1.

From equation (Eq. 4.23),

$$\nabla G(\boldsymbol{p},\boldsymbol{q})\cdot\hat{\boldsymbol{n}}_q = \frac{ik}{4}H_1^{(1)}(kr)(\hat{\boldsymbol{r}}\cdot\hat{\boldsymbol{n}}_q)\,, \tag{4.24}$$

and using this result, the coefficient matrices [L] and [M] become

$$L_{ij} = \int_{q_{j-1}}^{q_j} \frac{i}{4}H_0^{(1)}(kr)\,\mathrm{d}S \tag{4.25}$$

$$M_{ij} = \int_{q_{j-1}}^{q_j} \frac{ik}{4}H_1^{(1)}(kr)(\hat{\boldsymbol{r}}\cdot\hat{\boldsymbol{n}}_j)\,\mathrm{d}S\,. \tag{4.26}$$

It will be seen in Chapter 4.8 that these integrals can be computed numerically and in some limited cases analytically, in particular for the case of $i = j$. From this, (Eq. 4.15)

can be solved to find the surface potential ϕ for a given incident sound wave.

4.8 Integration methods

4.8.1 Numerical integration

The values of the coefficient matrices [L] (Eq. 4.13) and [M] (Eq. 4.12) can be computed by any number of numerical integration techniques. Due to the free choice of sample points available, the Gaussian Quadrature Integration technique was chosen as it provides the highest order of accuracy for a given number of points, and is easily implemented. Numerical results from the Hankel functions (Eq. 4.22) and (Eq. 4.23) can be computed easily by numerical programs such as MATLAB using in-built functions.

The general form of Gaussian Quadrature integration is (from Kreyszig [18])

$$\int_1^b f(x)\mathrm{d}x \approx \left(\frac{a+b}{2}\right)\sum_{j=1}^{n} w_j f(x_j) + R_n\,,$$

where x_j is a set of sample point locations, each with a corresponding weighting w_j. Sample locations and weights used have been published by Abramowitz and Stegun [4] and are listed in Appendix B.5. For a number of gaussian points n, the coefficient matrices [L] and [M] are calculated as

$$\mathrm{L}_{ij} = \frac{(q_j - q_{j-1})}{2}\frac{i}{4}\sum_{m=1}^{n} w_m H_0^{(1)}(kr_m) \tag{4.27}$$

$$\mathrm{M}_{ij} = \frac{(q_j - q_{j-1})}{2}\frac{ik}{4}\sum_{m=1}^{n} w_m H_1^{(1)}(kr_m)(\hat{\boldsymbol{r}}\cdot\hat{\boldsymbol{n}}_j)\,. \tag{4.28}$$

A notable property of the Hankel functions (Eq. 4.22) and (Eq. 4.23) is

$$\lim_{z\to 0} H_0^{(1)}(z) = \infty\,,\ \text{and}$$
$$\lim_{z\to 0} H_1^{(1)}(z) = \infty\,,$$

as shown in Figure 4.7.1. Due to this result, evaluating the Hankel function at the source location ($r = 0$) must be avoided. Rocchi [23] and Smith [28] avoided this problem through using an even number number of quadrature points across the element in order to avoid a quadrature point at the element midpoint. While this avoided calculating the

Hankel function at an undefined value, it was found that relatively large inaccuracies are obtained by using such numerical techniques across the asymptotic point of $r = 0$.

Another option for integrating the Hankel function across the source element is to use an analytical solution. This is discussed in the following Chapter 4.8.2.

4.8.2 Analytical integration

It is possible to analytically integrate the Hankel function across an element with the source at its midpoint, without encountering the difficulties involved when integrating across an element with an external source. This returns an exact result, and is a solution to the numerical integration errors around asymptotic points mentioned in Chapter 4.8.1.

The use of symmetry can be used about the centre of the element, with the identity

$$\int_{-l/2}^{l/2} G(kr)dr = 2\int_{0}^{l/2} G(kr)dr\,.$$

The integral of the Hankel function of the first kind order zero, is published by Abramowitz and Stegun [4] as

$$\int_0^x H_0^{(1)}(z)\mathrm{d}z = xH_0^{(1)}(x) + \frac{1}{2}\pi x\left(\mathbf{H}_0(x)H_1^{(1)}(x) - \mathbf{H}_1(x)H_0^{(1)}(x)\right)\,, \tag{4.29}$$

where $\mathbf{H}_\nu$ is the Struve function of order ν. While MATLAB has a built-in Hankel function, it does not have a built-in Struve function, which had to be evaluated from its series form. The Struve function has the form

$$\mathbf{H}_\nu = \left(\frac{z}{2}\right)^{\nu+1}\sum_{k=0}^{\infty}\frac{(-1)^k(\frac{z}{2})^{2k}}{\Gamma(k+\frac{3}{2})\Gamma(k+\nu+\frac{3}{2})}\,. \tag{4.30}$$

Here Γ is the Gamma function, and $\Gamma(n+\frac{1}{2})$ is defined by Abramowitz and Stegun [4] as

$$\Gamma(z) = \int_0^\infty t^{z-1}e^{-t}\mathrm{d}t \quad (Re(z) > 0)\,, \tag{4.31}$$

with the identities

$$\Gamma\left(n+\frac{1}{2}\right)=\frac{1\cdot 3\cdot 5\cdot 7\cdot \ldots (2n-1)}{2^n}\Gamma(\frac{1}{2})\,, \tag{4.32}$$

and

$$\Gamma\left(\frac{1}{2}\right)=\sqrt{\pi}\,. \tag{4.33}$$

In order to make use of (Eq. 4.29) to evaluate (Eq. 4.25), the variable of integration must be changed, as

$$\int_0^{l/2} H_0^{(1)}(kr)\,\mathrm{d}r=\int_0^{lk/2}\frac{H_0^{(1)}(kr)}{k}\,d(kr)\,. \tag{4.34}$$

It follows that we can analytically calculate an exact solution of the Hankel function $H_0^{(1)}$ integral across the source element as

$$\int_{-a}^{a} H_0^{(1)}(kr)\mathrm{d}r=\frac{2a}{k}H_0^{(1)}(a)+\frac{\pi a}{k}\left(\mathbf{H}_0(a)H_1^{(1)}(a)-\mathbf{H}_1(a)H_0^{(1)}(a)\right)\,,\ a=kl/2\,. \tag{4.35}$$

While this provides a substantial improvement in accuracy, this also improves the efficiency of obtaining a solution, as discussed in Chapter 5.2.1.

It is not necessary to evaluate a solution for [M] across the source element, as

$$(\hat{\boldsymbol{r}}\cdot\hat{\boldsymbol{n}_j})=0,$$

due to $\hat{\boldsymbol{r}}$ and $\hat{\boldsymbol{n}_j}$ existing perpendicular to one another (refer to Eq. 4.26). Therefore the diagonal elements of [M] will always be 0.

Chapter 5

BEM Code Development and Optimisation

This Chapter details the development of the BEM code, in particular for the purposes of modelling Schroeder diffusers. Chapter 5.1 outlines the methods used to increase the speed and accuracy of the solution. Chapter 5.2 validates the code and quantifies the improvements made.

5.1 Techniques

5.1.1 Improvement of receiver solution calculation

In developing the code, a small error was resolved that resulted in incorrect receiver locations. Redundant sub-functions were also removed and the efficiency of applying the solution to off-surface nodes was increased.

5.1.2 Code structure

Improvements were made to the structure in most code subroutines to increase the efficiency and decrease running time. Where possible, vectors, arrays and matrices were pre-allocated, as suggest by MathWorks [20]. Function handles were also declared outside of loops, which resulted in large improvements in the relevant section runtime. Where possible, repeating loops were replaced with vectorised equations. In particular, the innermost loop of nested loops was vectorised, to effectively reduce the number of nested loops by one. Some built-in MATLAB functions such as the dot product function were replaced with code capable of efficient vectorised calculations. When calculating values for matrices that are symmetrical about the diagonal axis such as those used to allocate the number of Gaussian quadrature points for pairs of elements, one half of the

matrix was calculated and then the matrix was reflected across the diagonal axis. Separate functions were written for calculations with different BEM inputs, such as frequency band modelling, to take advantage of increased efficiency opportunities.

5.1.3 [M] and [L] coefficient matrix creation

The vast majority of the program runtime is creation of the coefficient matrices [M] and [L]. As described in Chapter 4.8.1, the function written by Rocchi and Smith numerically integrated each element with respect to each other element using 20 Gaussian points. For a geometry of n elements, this results in $40n^2$ integration points evaluated to create [L] and [M]. The following steps were implemented to increase the efficiency and accuracy:

1. **Analytical computation of $\mathbf{M}_{ii}$ and $\mathbf{L}_{ii}$ elements**.

   As described in Chapter 4.8.2, an analytical integral of the Hankel function of the form

   $$\int_{-a}^{a} H_0^{(1)}(kr)\mathrm{d}r = \frac{2a}{k}H_0^{(1)}(a) + \frac{\pi a}{k}\left(\mathbf{H}_0(a)H_1^{(1)}(a) - \mathbf{H}_1(a)H_0^{(1)}(a)\right),$$

   was used to compute diagonal matrix terms in the surface element matrices. When implemented, this resulted in large accuracy increases. The analytic solution was also quicker to compute than a numerical solution, resulting in speed improvements for diagonal matrix terms.

2. **Decreased number of Gaussian Quadrature points for increasing distance between element pairs.**

   Figure 4.7.1 shows the decrease in absolute value of the Hankel functions with increasing r. It follows that errors in the numerical integration of the Hankel functions with larger r will be greater than those with smaller r, and will lead to larger end-result errors. This is of most importance when calculating the [M] and [L] matrices for surface pressures, as large differences in r are encountered, from adjacent elements to elements at opposite sides of a diffuser. For these matrices, the code was modified to set multiple threshold values for r, with decreasing

numbers of Gaussian Quadrature points for element pairs with increasing distance between. Table 5.1.1 shows values found to produce a balance of high accuracy and decreased runtime. However, these values could be subject to further optimisation.

Table 5.1.1: r threshold values and Gaussian Quadrature points.

$r = \lvert\boldsymbol{p} - \boldsymbol{q}\rvert$	**Gaussian Quadrature points**
$r < \frac{\lambda}{2}$	10
$\frac{\lambda}{2} < r < \lambda$	6
$\lambda < r < 3\lambda$	4
$3\lambda < r$	2

During diffusion modelling, the radius of off-surface receivers can usually be considered to be much larger than the diffuser geometry. It follows that the distance between receivers and elements is relatively consistent, and the accuracy of certain element-receiver pairs cannot be prioritised as was done for surface element pairs above. For a model of n elements and m receivers, surface element matrices [M] and [L] have dimensions [n,n] while the off-surface receiver matrices are of size [n,m]. For constant m and varying n, which is common in diffusion modelling, the size of surface matrices are proportional n^2 whereas the size of receiver matrices are linearly proportional to n. Combined with the assumption for large models $n >> m$, the calculation efficiency of off-surface receiver matrices is less critical than the calculation of surface matrices. Numerical integration using 10 Gaussian Quadrature points for off-surface receiver matrices was found to deliver a balance between efficiency and accuracy.

3. **Increased Gaussian Quadrature points for pairs of corner elements.**

Figure 4.7.1 shows the absolute value of $H_1^{(1)}(kr)$ increases in value at a higher rate than $H_1^{(0)}(kr)$ with decreasing r, and from Chapter 4.7,

$$\mathrm{M}_{ij} = \int_{q_{j-1}}^{q_j} \frac{ik}{4} H_1^{(1)}(kr)(\hat{\boldsymbol{r}} \cdot \hat{\boldsymbol{n}_j})\,\mathrm{d}S\,.$$

For pairs of elements adjacent and parallel, $(\hat{\boldsymbol{r}} \cdot \hat{\boldsymbol{n}_j}) = 0$, however for a pair of elements on opposing sides of a corner, $(\hat{\boldsymbol{r}} \cdot \hat{\boldsymbol{n}_j}) \neq 0$, and assuming elements are the same length and perpendicular, this would equal between 0.438 and 1.

To minimise corner errors in the coefficients M_{ij}, 20 Gaussian Quadrature points are used when i and j are within the first three elements adjacent to a corner on opposing sides.

5.1.4 Element edge size refinement

The method of discretisation used in this implementation of the BEM uses the simplification of constant ϕ across each element, as discussed in Chapter 4.1. Therefore, one of the conditions needed to model an object accurately is to have the element size small enough to accurately represent the change in ϕ across a surface. To increase the accuracy and/or decrease the number of elements needed for a given level of accuracy, the element size can be decreased in regions with a high ϕ gradient, $\frac{\partial \phi}{\partial l}$ and increased in sections with a lower gradient. Figure 5.1.1 shows the surface pressures of an infinite square column, and high pressure gradients at locations of close proximity to prism edges are clearly visible. This effect was also tested for an $N = 7$ QRD shown in Figure 5.1.2, where the colour bands represent the magnitude of the pressure gradient $|\frac{\partial P}{\partial l}|$. It is clear from these two tests that edges represent areas of interest with respect to surface pressures, and the corner element size may be a limiting constraint on the accuracy of a BEM model.

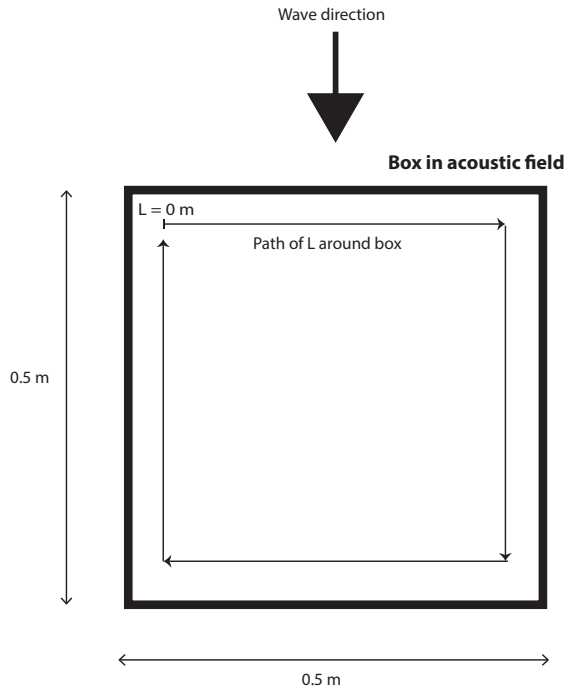

(a) Test diagram

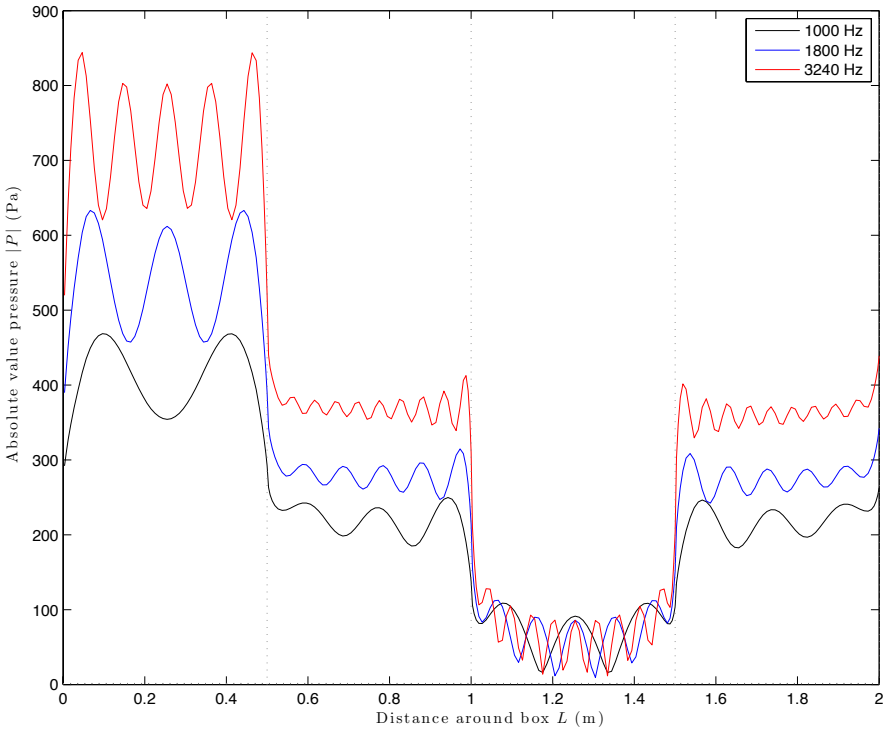

(b) Surface pressures. Vertical dotted lines represent corner locations.

Figure 5.1.1: Surface pressures of an infinite square column in a point source acoustic field. Box dimensions $0.5 \times 0.5\,\mathrm{m}$.

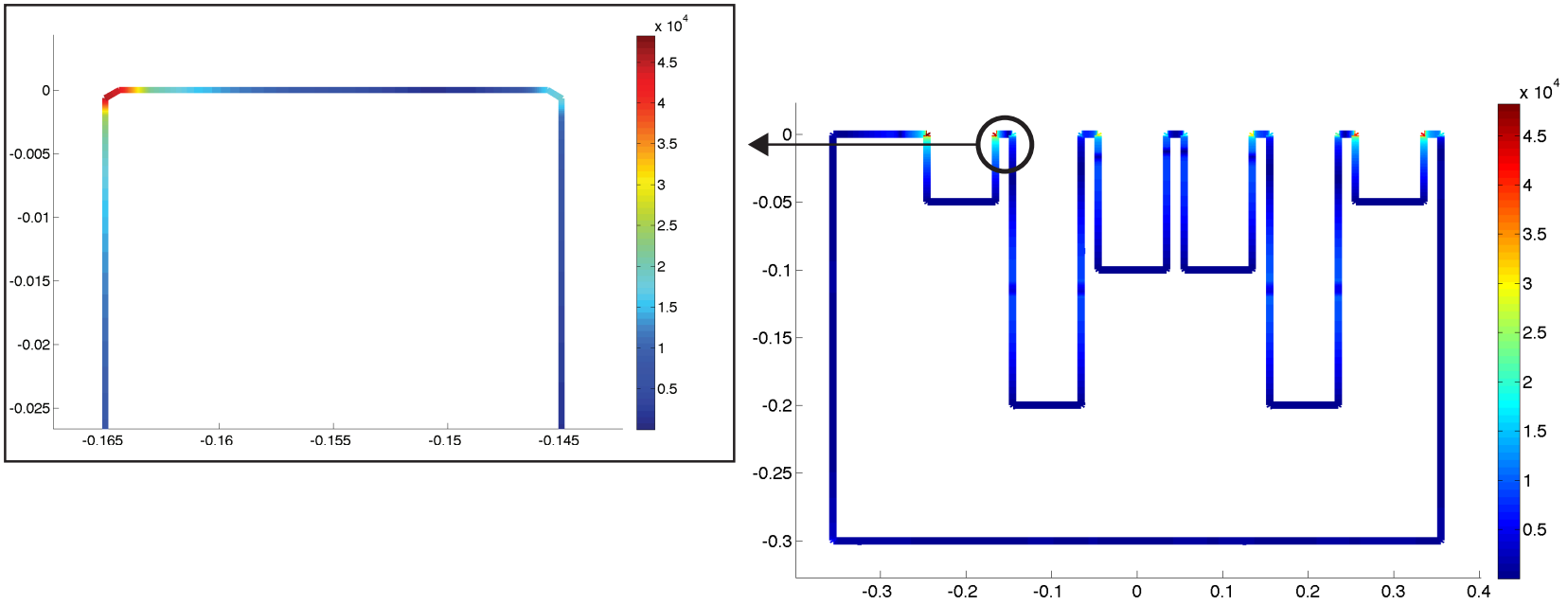

Figure 5.1.2: QRD surface pressure gradient magnitude $|\frac{\partial P}{\partial l}|$ (Pa/m). $N = 7$ QRD, $w_T = 0.7$ m, $d_{\max} = 0.3$ m, 1000 Hz.

To achieve a higher resolution of surface pressures near edges, the BEM code was modified to include an option to reduce the element size at elements adjacent to edges, with subsequent element sizes increasing by a common factor until reaching a maximum element size. The edge refinement discretisation code has a user specified value for the edge-adjacent size e_{edge}, maximum element size e_{max} and number of inflation layers n. Element sizes in the refined region extending from an edge are then calculated as

$$e_i = e_{\text{min}} \times \alpha^{i-1}, \; i = [1, n] \tag{5.1}$$

where $\alpha = \left(\frac{e_{\text{edge}}}{e_n}\right)^{1/n}$, and e_{min} and e_n are both scaled by a similar factor to allow a perfect fit between to edges, such that $e_{\text{min}} \leq e_{\text{edge}}$ and $e_n \leq e_{\text{max}}$.

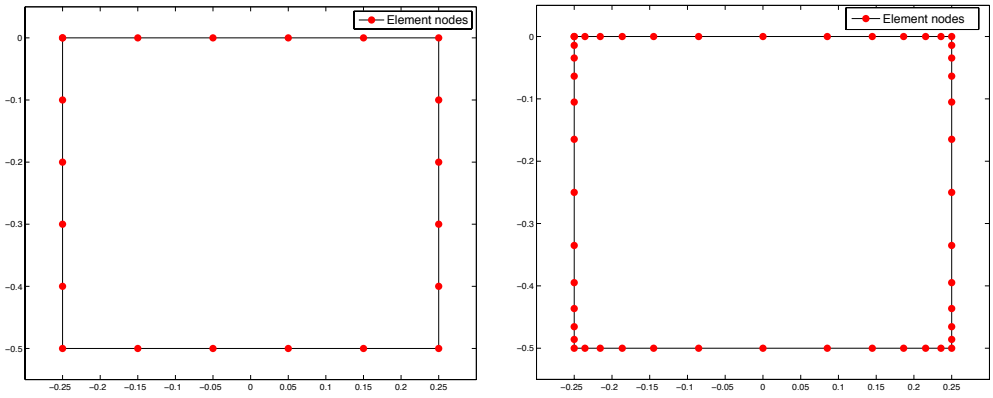

(a) Without edge refinement (b) With edge refinement

Figure 5.1.3: Infinite square column discretisation with and without edge refinement. Square dimensions 0.5×0.5, $e_{\text{max}} = 0.1$, $n = 5$, $e_{\text{edge}} = 0.2$.

5.1.5 Fix for non-unique BEM solutions

As mentioned in Chapter 2.5.1.2, non-unique solutions from BEM models are rare but possible due to the eigensolutions of the geometry interior. A simple method to check whether an abnormal solution may be attributed to this problem was developed with the BEM code. A correct solution should not be altered by the presence of a hollow cavity of arbitrary dimensions within the diffuser geometry model. The effect of the hollow cavity however will alter the eigensolution of the geometry interior, and if the initial solution was a non-unique solution, the introduced cavity would be expected to correct it. An example of a diffuser geometry model with a hollow cavity is shown in Figure 5.1.4. It was found that all tests were highly similar when tested with and without an internal

cavity, likely suggesting that non-unique solutions were not a problem during modelling. However, a result of a non-unique solution was not encountered during testing, so the effectiveness of this method could not be verified.

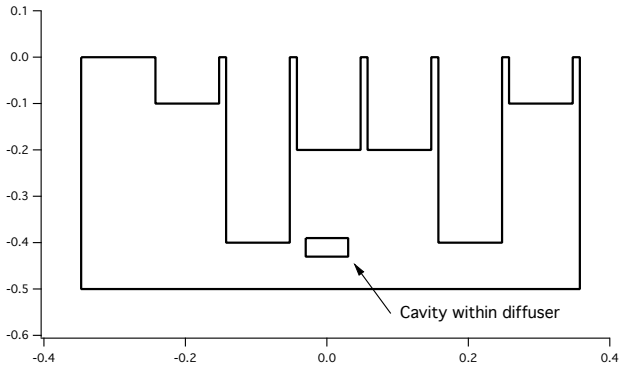

Figure 5.1.4: QRD model with hollow cavity to check for non-unique solutions. $N = 7$ QRD, $Nw_{_T} = 0.7$ m, $d_{\max} = 0.4$ m, $P = 1$.

It should be noted that the normal vectors of the hollow cavity must face outwards from the diffuser surface. Due to this, the cavity corner points must be listed in a clockwise direction for the MATLAB function to correctly calculate normal vectors facing outwards from the diffuser surface, whereas the external corner points are listed anti-clockwise for outwards facing normal vectors.

5.2 Code Optimisation and Development Results

5.2.1 Overview

Performance testing was conducted on the current BEM code to both validate the results, and measure the increase in speed and accuracy when compared to the original code. Validation done in two parts: the first compared pressure diffusion results from a BEM model to a simple case where there exists an analytical solution (Chapter 5.2.2). The second part considered more complex and realistic diffuser geometry including QRDs, and includes validation against other published results (Chapter 5.2.3), and solution convergence testing for a wider range of problems (Chapter 5.2.5.2).

The improvement in code performance is tested for two cases: an infinite cylinder and a QRD. The solution time and accuracy are compared for both. A detailed accuracy study of the current code is included, including the relationship between thin panels thickness, element size, frequency, geometry and error.

5.2.2 Comparison to analytic solution

The exact diffusion from an infinite cylinder can be modelled using the analytic solution from Morse & Ingard [21]

$$\left|\frac{p_d}{p_0}\right| = \sum_{m=0}^{\infty} A_m \cos(m\theta) H_m^{(1)}(kr)\,, \tag{5.2}$$

where

$$A_m = -\epsilon_m i^{m+1} e^{-i\gamma_m} \sin\gamma_m\,, \qquad \epsilon_0 = 1,\ \epsilon_m = 2 \text{ for } m > 0\,,$$

$$\gamma_0 = \arctan -\frac{J_1(ka)}{Y_1(ka)}\,, \qquad \gamma_m = \arctan \frac{J_{m-1}(ka) - J_{m+1}(ka)}{Y_{m+1}(ka) - Y_{m-1}(ka)}\,,$$

and θ is the angle from wave approach direction. This solution can be compared to results from discretisation modelling methods such as the BEM for error analysis. Values of ka and kr are used to represent the nondimensionalised radius of a cylinder and off-surface receiver arc respectively, as shown in Figure 5.2.1.

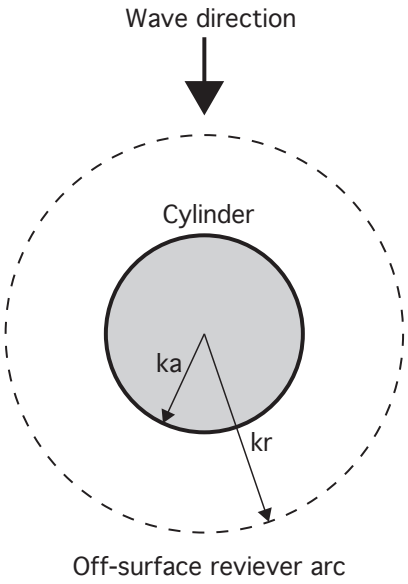

Figure 5.2.1: Diagram of diffusion model from an infinite cylinder.

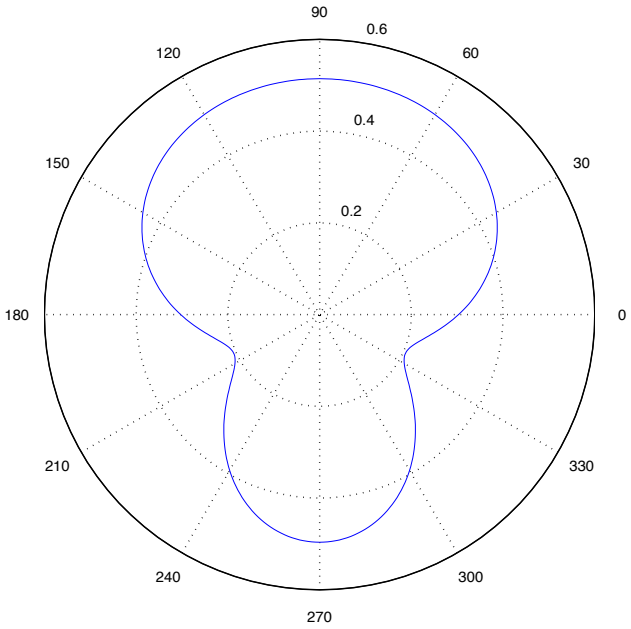

Figure 5.2.2: Diffusion from a cylinder due to a plane wave, normalised to the incident wave strength. $ka = 1$, $kr = 2$.

The current BEM code, original BEM code and analytic solution were used to calculate off-surface pressures at 360 evenly spaced receivers around a cylinder with $ka = 1$, $ka = 2$, 360 surface elements in a plane wave incident field. Figure 5.2.2 shows the diffusion polar response from this test, and Table 5.2.1 shows an error comparison between the three sets of results. Errors are calculated as a percentage of the average value. The optimised code is on average approximately 200 times more accurate than the original code. It should be noted that the level of accuracy shown for the case of an infinite cylinder is not necessarily applicable to other geometry. More common and complex diffuser geometries such as QRDs are likely have larger errors due to the effects of sharp corners and thin panels. This is discussed in Chapter 5.2.5.

Table 5.2.1: Comparison of receiver pressure error when compared to an analytical solution. Error is calculated as a percentage of the average value. Test geometry is an infinite cylinder with $ka = 1$, $kr = 2$, 360 receivers, 360 surface elements in a plane wave incident sound field.

	Original	**Optimised**	**Improvement**
Average error (%)	0.259	0.00127	20285%
Max error (%)	0.696	0.00289	24062%

5.2.3 Comparison to published diffusion data

The infinite cylinder modelled above is comparable in size to the wavelength, symmetrical about all axis and contains no thin panels. In comparison, common diffuser geometry can be much larger, asymmetrical, and contain thin protruding panels. For this reason, the BEM code is further validated against complex diffuser geometry, in particular QRDs.

Figure 5.2.3 shows a comparison of the predicted diffusion polar plot of a 6 period $N = 7$ QRD at six times the design frequency. Modelling by Cox & D'Antonio does not specify the method used. The location of lobes are marked on each polar plot and are highly consistent across the two figures. Relative magnitudes are also consistent at angles between approximately $\pm 45°$ from the from the normal to the diffuser surface, however differences are observed at acute angles. Explanations for this may be that values from Cox & D'Antonio are normalised to incident acoustic field at receiver locations,

or were modelled using the Kirchoff method which becomes less accurate for scattering at acute angles due to its inability to model second order reflections [7]. The similarities in lobe position are a strong validation of the BEM code accuracy when modelling diffusion polar patterns.

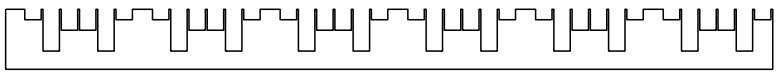

(a) QRD geometry

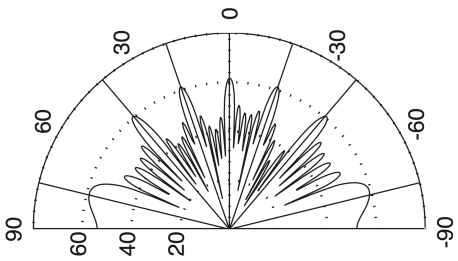

(b) Cox & D'Antonio [7]

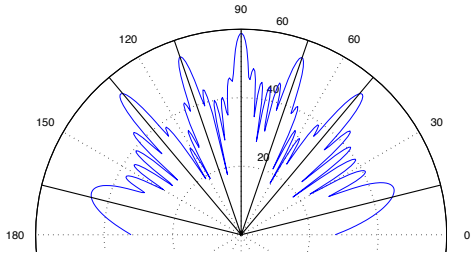

(c) BEM program

Figure 5.2.3: Comparison of diffusion lobe positions (dB) for an $N = 7$ QRD at 3000 Hz, $P = 6$, $f_0 = 500$ Hz. Solid radial lines represent angles of $\pm 19°$, $\pm 40°$, $\pm 78°$ and $90°$ relative to the diffuser length. Note that although the axis are labelled differently, the sound wave approaches from above in both figures.

Figure 5.2.4 shows a comparison of the diffusion coefficient (as defined in Chapter 2.3.3.1) across a frequency range from a 6 period QRD, as modelled by Cox & D'Antonio and using the BEM as part of this work. Values are taken from an average of seven tests at logarithmically spaced frequencies across third octave bands. Modelling by Cox & D'Antonio used the BEM thin panel solution (as described in Chapter 2.5.2.1) and modelled the diffuser with an open back, while the test results from this work did not use the thin panel solution and modelled a closed-back diffuser. Basic geometry was given by Cox & D'Antonio. However, some details were not specified and were estimated for this work. Smaller elements were also used than the maximum size specified by Cox & D'Antonio of $\frac{\lambda}{8}$. There is a strong correlation between the two sets of data, and differences can be attributed to slight differences in geometry, the thin panel solution, and different element sizes used during testing.

The relatively high level of diffusion at the 100 Hz third-octave band from Cox & D'Antonio is surprising, as the expected normalised diffusion coefficient at this frequency

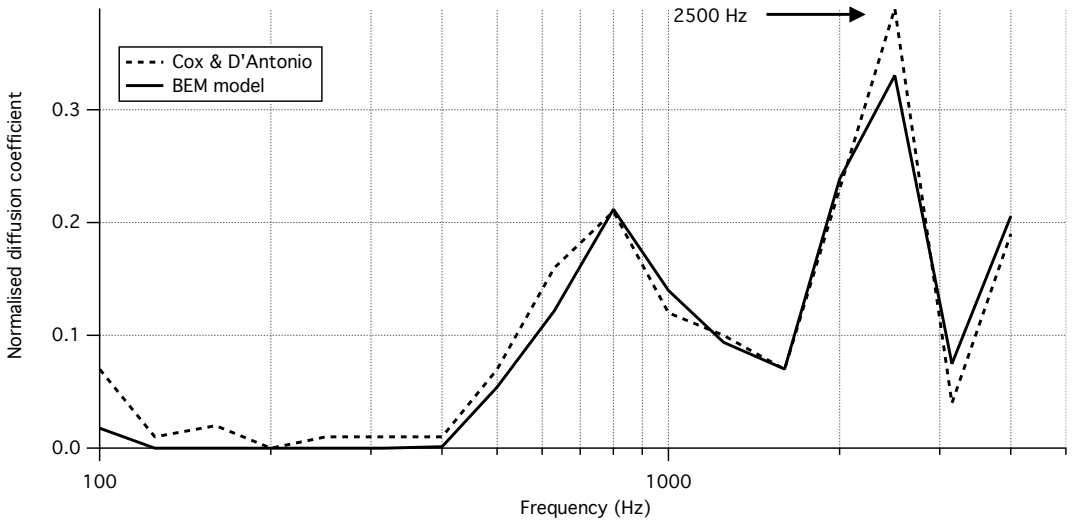

Figure 5.2.4: Comparison of normalised diffusion coefficients between values published by Cox & D 'Antonio [7] and BEM program. $N = 7$ QRD, $P = 6$, $Nw_T = 0.6$ m, $d_{\max} = 0.2$ m.

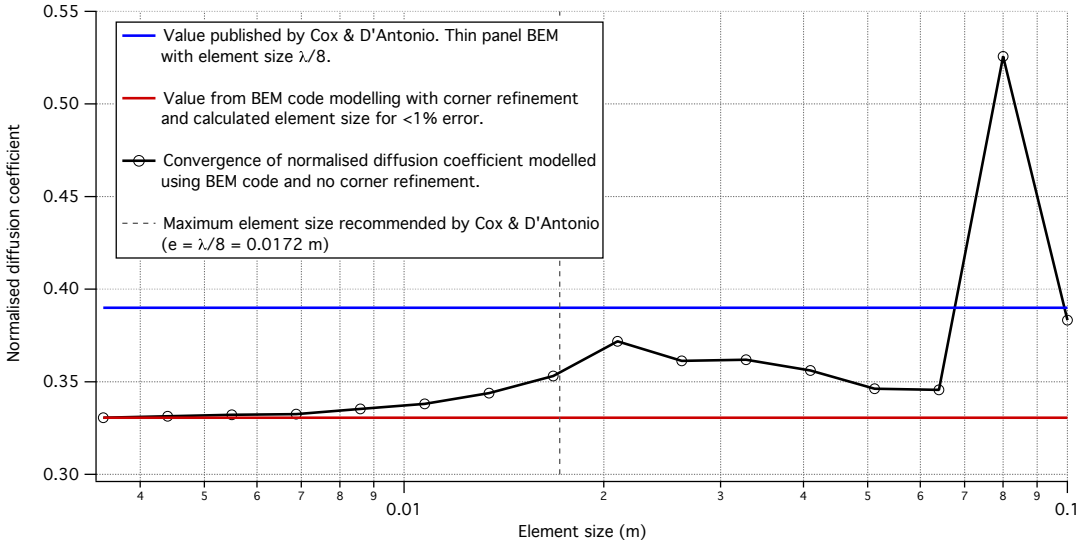

Figure 5.2.5: Convergence of diffusion coefficient at 2500 Hz for QRD as modelled in Figure 5.2.4

would be very close to 0. It is likely that differences at high frequencies can be partially attributed to the thin panel assumption, where at 3000 Hz the panel thickness represents approximately 10% of the wavelength and reflection occurring from the panel tips will not be modelled using the thin panel solution. The largest difference in diffusion coefficients can be seen at the 2500 Hz frequency band, where the difference between results is 17% of the modelled value from this work. 2500 Hz represents $5 \times f_0$, so significant diffraction lobes could be expected (see Chapter 2.4.3.2), and a suitably small element size may be needed to accurately model these lobes.

To verify the solution convergence at this frequency band, the diffusion coefficient was calculated using the BEM code with decreasing element sizes, shown in Figure 5.2.5. The value shown in blue is taken from Cox & D'Antonio, and the value shown in red was calculated from the BEM code using edge element size refinement (see Chapter 5.1.4), and an element size with estimated error below 1% (see Chapter 5.2.5.2). The convergence line shown in black does not use edge element size refinement, and shows diffusion coefficient convergence with decreasing element size. The broken line indicates the element size $\frac{\lambda}{8}$ recommended as the maximum size by Cox & D'Antonio, and it is clear the solution at this element size has not fully converged. The value of 0.331 calculated from this work appears very close to the convergence trend value. From this, the solution derived from BEM modelling can be assumed to be accurate, and the difference in the value published by Cox & D'Antonio can be attributed to geometry differences, the thin panel solution, and possibly the effect of different element sizes.

5.2.4 Timing improvements

Figure 5.2.6 shows the timing improvement between the original and current code for the case of the infinite cylinder shown in Figure 5.2.1, with $ka = 1$, and $kr = 2$. The number of surface elements and receivers were similar, and increased by a factor of 2 each test. As would be expected, there is an exponential increase in the reduction in runtime with an increasing number of elements. On average, the optimised code was approximately 46 times faster than the original code.

Figure 5.2.7 shows comparison between three BEM codes: Code 1 is the original BEM code, Code 2 is the current code without element edge refinement, and Code 3 is the current code with element edge refinement. A QRD array of $P = 3$ was modelled

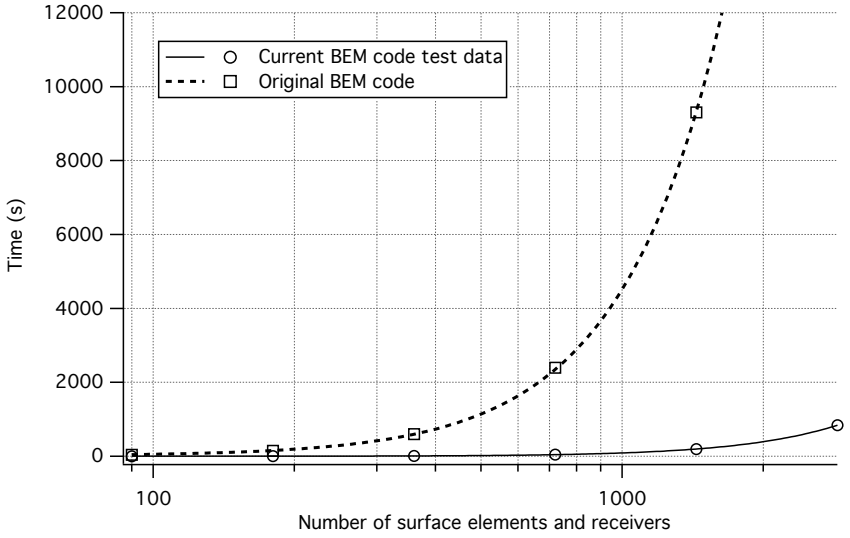

Figure 5.2.6: Timing comparison between original and optimised code. Model of an infinite cylinder with a similar number of surface elements and receivers, $ka = 1$, $kr = 2$.

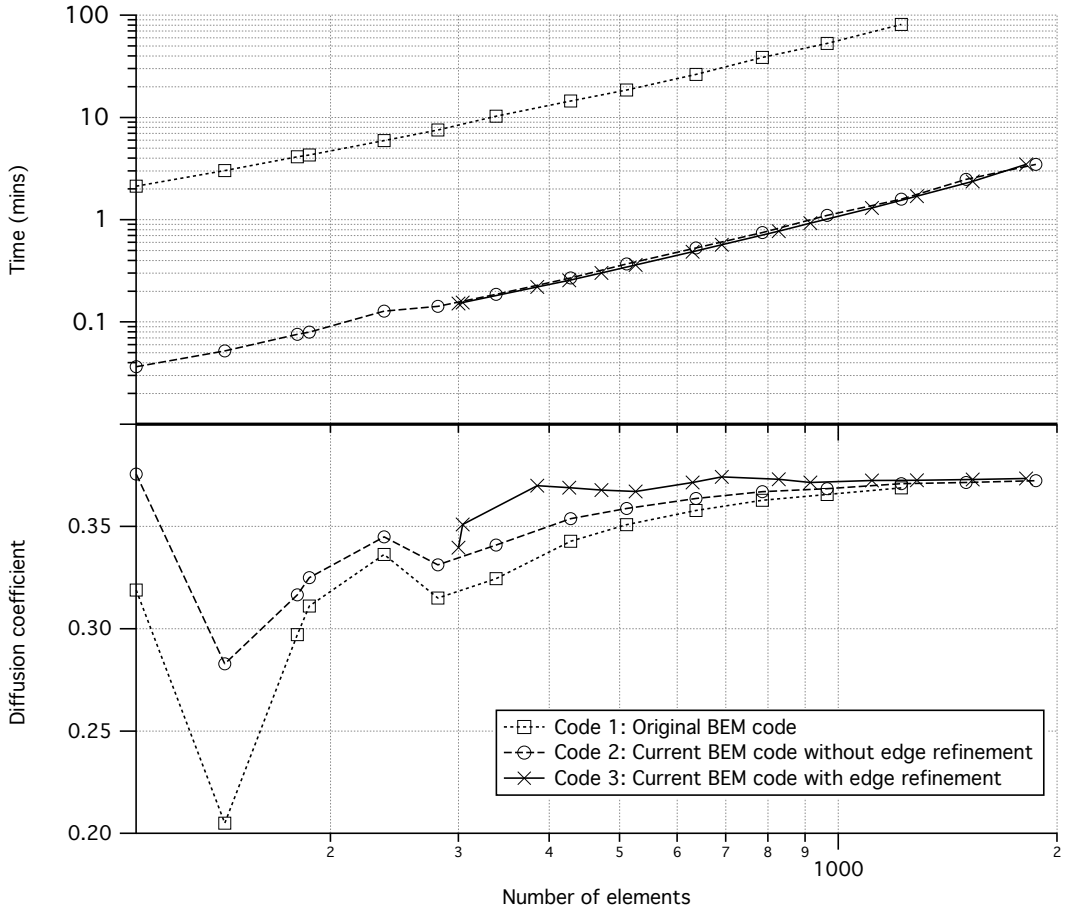

Figure 5.2.7: Comparison of solution time and convergence from 3 BEM code versions. $N = 7$ QRD, $P = 3$, $(Nw_T) = 0.56$ m, $d_{\max} = 0.196$, $f = 2000$ Hz ($f = 4f_0$).

at $f = 4f_0$ with each code and with varying element sizes. Large speed improvements are evident between original and current BEM codes, with an average speed difference of over 50 times faster for similar numbers of elements. For a solution within ±1% of the converged value, Code 3 required a model with 630 elements taking 29.2 s, Code 2 required 1221 elements taking 95.2 s, and Code 1 was not able to solve a solution within ±1% without excessive running times that could not be tested. At the minimum element size tested, Code 3 required 81 minutes (4876 s) to produce a solution within 1.23% of the converged value. This comparison is very significant, and confirms that the current BEM model offers large speed and accuracy increases, both from refined discretisation methods and numerical calculation improvements.

A breakdown of timing improvements for the code at three stages of optimisation is shown in Table 5.2.2. The majority of timing improvements are achieved during the coefficient matrix [M] and [L] creation, and affect both the number of loops required and the speed of loop calculations. In this way, the total timing improvement is approximately equal to a product of the individual improvements. Stages 1, 2 and 3 correspond to:

1. Improving the integration methods used in calculating [M] and [L] (Chapter 5.1.3).
2. Replacing loops and built-in MATLAB functions with vectorised equations (Chapter 5.1.2).
3. General code restructuring, including variable declaration and declaring function handles outside loops. Replacing nested 'if' statements with loops.

Table 5.2.2: Solution time improvements breakdown

Diffuser type	**Stage 1**	**Stage 2**	**Stage 3**	**Total**
Infinite cylinder $ka = 5,\ kr = 10$	21.6%	820%	341%	4931%
QRD $N = 7,\ P = 1\,,\ f = 1000Hz$	26.0%	824%	332%	5032%
QRD $N = 7,\ P = 3\,,\ f = 2000Hz$	37.0%	1039%	250%	5460%

The timing improvements shown allow for much larger and more detailed models to be run within a reasonable amount of time, and also allow for frequency-band averages

and frequency response testing without excessive running times. Speed improvements are increased when testing frequency-band averages, as the optimised code repeats only the necessary processes for each frequency, where others such as geometry creation, geometry discretisation and vector calculations are calculated only once per frequency band. In this work, diffusers were modelled and compared to a flat plate of similar dimensions at 7 points within each one-third octave band, at 18 one-third octave bands from 100 - 5000 Hz. This results in a total of 252 BEM simulations, 126 of the diffuser and 126 of a reference flat plate. For a 3 period $N = 7$ QRD array, the optimised BEM code can complete this full frequency test in less under two hours using element sizes with estimated error much less than 1% (see Chapter 5.2.6). For geometry with greater total length or numbers of wells, a full frequency response may take longer.

Information on the computer used during code testing is shown in Appendix B.4.

5.2.5 Element size, accuracy and convergence

Cox and D'Antonio [7] suggest that the desired level of accuracy needed for proper representation of the surface pressures can be reached with an element size of $\frac{\lambda}{8}$ or smaller for complex shapes. Convergence studies were conducted for many QRDs with varying frequency, periods, and well panel width to provide a guide to element size needed to produce a reasonable level of accuracy. The diffusion coefficient c_d was chosen as a quantitative single value diffusion result for convergence and accuracy testing, as it incorporates all polar point results. Convergence was tested by holding all variables constant except element size, and running models with decreasing element sizes. This was repeated for different parameters, and c_d was recorded for each element size. Error was calculated from what could be deemed the "correct solution". For highly converged trials this was taken as the result from the test with smallest element size, and for other cases the data was extrapolated to gain a solution when the element size tended to zero. Throughout the convergence testing, it was noted that the accuracy of which a "correct solution" could be determined was variable and inconsistent. Anomalies and inconsistencies were also present in some the convergence trends.

Exact multiples of frequencies were avoided so that if a frequency were critical in relation to some aspect of the diffuser geometry, this would not be repeated for consequent multiples of that frequency. A multiplying factor of 0.8 was used to determine

testing frequencies. During the convergence and accuracy testing, it was found there were predominantly two separate factors that influenced the level of accuracy:

1. The thickness of thin protruding panels resulting in errors due to the misalignment of elements on each side, as discussed in Chapter 2.5.2.1. A minimum element size is needed to avoid these errors and is a function of thin panel thickness only and not frequency.

2. For solutions at element sizes below those needed to avoid thin panel errors, a combination of frequency, geometry and element size affect accuracy. For a combination of these variables, maximum bounds for error can be estimated from convergence trends.

Both of these factors are discussed in the following sections.

5.2.5.1 Thin panel errors

As discussed in Chapter 2.5.2.1, thin protruding panels can lead to errors in the Boundary Element Method due to the alignment of elements on each side, and the approximation of a constant surface pressure across each element. This was found to be largely dependent on the geometry and less so on frequency. Tests were run with varying panel thickness w_P. An example is shown in Figure 5.2.8, where oscillating errors due to thin panels are present at smaller element sizes for thinner panels. The element size for which oscillating

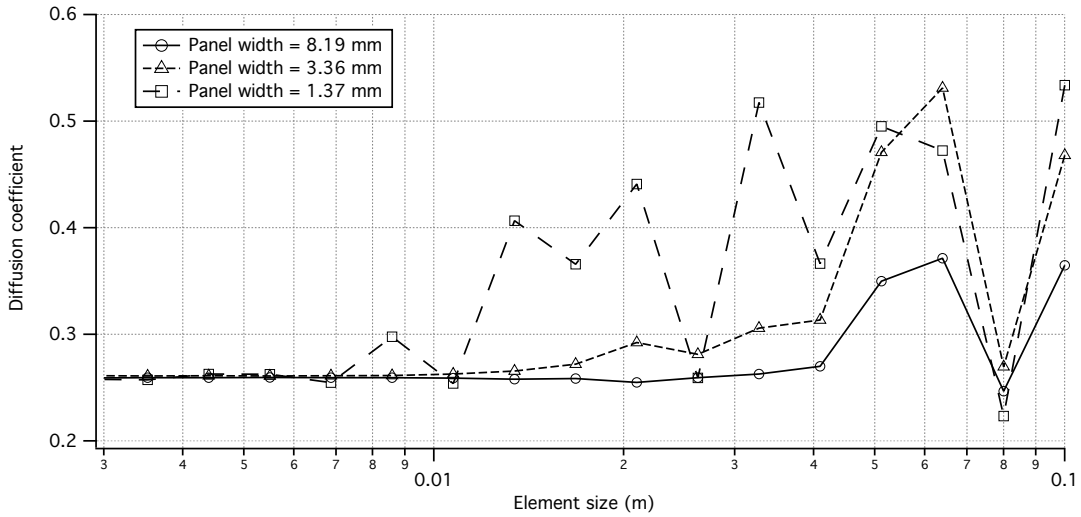

Figure 5.2.8: Example of convergence testing with varying panel width with for $N = 7$ QRD. $P = 3$, $Nw_T = 0.7$ m, $d_{\max} = 0.3$ m, $f = 3000$ Hz.

thin panel errors are not visible was recorded during convergence tests and the data are presented in Figure 5.2.9. Also shown is a curve with the equation

$$\text{Maximum element size} = 2.5 \times w_P,$$

for which all data points are above. This represents the relationship between maximum element size and panel thickness, for which confidence can be had that in most cases thin panel errors will not affect results.

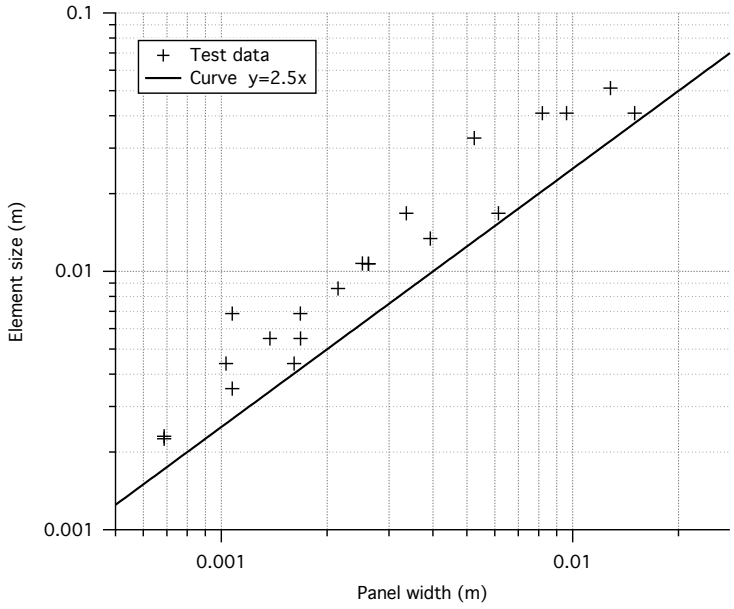

Figure 5.2.9: Maximum element size for which convergence errors are not dominated by thin panel errors.

5.2.5.2 Solution convergence

For element sizes less than those needed to avoid large errors thin panels, the convergence of a solution can be broadly represented by

$$\mathrm{E} < k \times e^m \tag{5.3}$$

where E is an upper bound for percentage error, k and n are constants, and e represents element size. During testing it was found that for models with an acoustic wave approaching normal to the diffuser, convergence was related predominantly to frequency, total well width w_T and the total number of wells n_w. $n_w w_T$ can also be written as the total diffuser length. A dimensionless variable e_{norm} was created to describe the

relationship between element size, frequency and diffuser well width. e_{norm} is defined as

$$e_{\text{norm}} = \frac{1}{\sqrt{20}} \sqrt{0.336 \left(\frac{e}{w_T n_w} \right)^2 + \left(\frac{ef}{c} \right)^2} \tag{5.4}$$

where the coefficients were determined through convergence testing of different frequencies and diffuser geometries. For comparison of different diffuser geometries and frequencies, e_{norm} can be substituted into the inequality (5.3), and taking the logarithm of both sides gives

$$\log_{10}(\text{E}) < m \log_{10}(e_{\text{norm}}) + k \,. \tag{5.5}$$

From a plot of $\log_{10}(\text{E})$ against $\log_{10}(e_{\text{norm}})$, linear trends of gradient m and y-intercept k would be expected. An example of this is shown Figure 5.2.10 where convergence tests were run for three QRD diffusers as listed in Table 5.2.3, all with total width = 2.4 m, panel width of $0.1w$. These convergence trends were repeated at 500, 900, 1620, 2916 and 5249 Hz. A best fit upper limit for error is shown, and has the equation

$$\text{E} < 631 \times {e_{\text{norm}}}^{1.5} \,.$$

From this and the definition of e_{norm}, the element size needed for a desired level of accuracy can be determined as

$$e_{\text{max}} = \frac{1}{\sqrt{20}} \sqrt{\frac{\left(\frac{\text{E}}{631}\right)^{\frac{2}{1.5}}}{\left(\frac{0.048}{{w_T}^2 {n_w}^2}\right) + \left(\frac{f}{c}\right)^2}} \,. \tag{5.6}$$

As seen in Figure 5.2.10, the rate of convergence is variable for different geometries and

Table 5.2.3: QRD details for convergence testing, as shown in Figure 5.2.10

	Test 1	**Test 2**	**Test 3**
Design frequency f_0 (Hz)	500	1000	2000
Max depth d_0 (m)	0.196	0.0981	0.0490
Period width Nw_T (m)	0.8	0.6	0.4
Number of periods P	3	4	6

frequencies. In general, it was found that tests in which a critical dimensions such as period length or well depth was approximately equal to a small multiple of wavelength

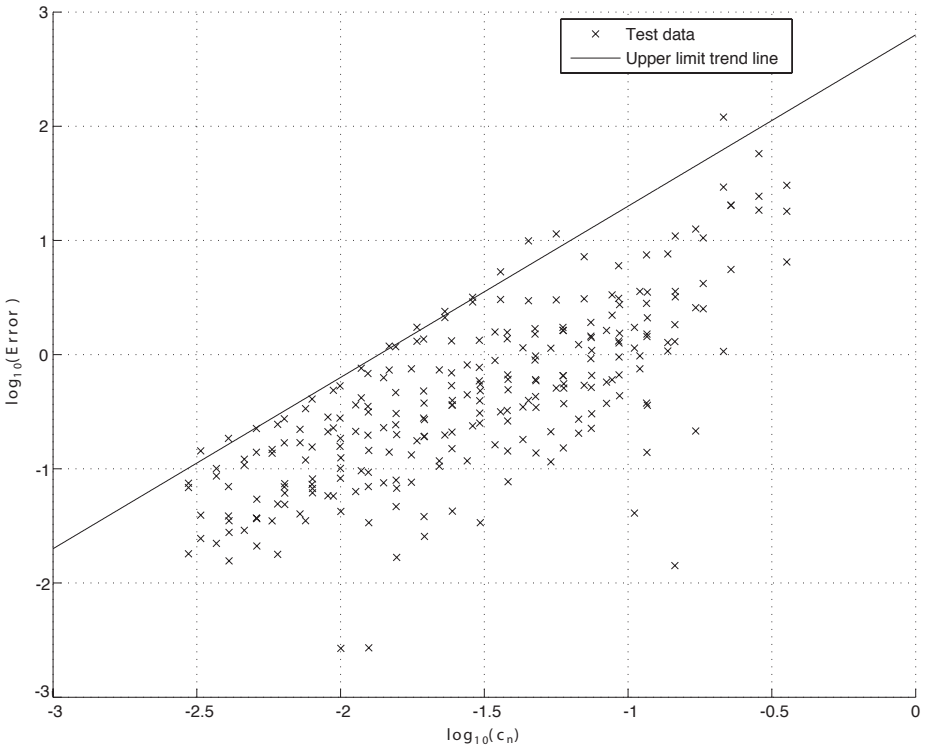

Figure 5.2.10: Convergence study with normalised element length e_n, shown on a log-log scale.

experienced slower convergence. Also experiencing slower convergence were polar diffusion patterns with large narrow spikes and diffusers with all well depths a multiple of $\lambda/2$ (see Chapter 2.4.3.2), both of which involve large amounts of constructive and destructive interference between between reflections. It can be concluded that these situations require small element sizes to be modelled to a high degree of accuracy.

The curve shown in Figure 5.2.10 was applied so that the slowest converging solutions have error below this point, and hence Equation (5.6) is an effective method for calculating the necessary element size for an approximate upper error bound. It was noted however that the element sizes as specified by this relationship in some instances are substantially smaller than necessary, in particular for QRD models of larger well widths at high frequencies. In the absence of additional convergence information, element sizes as specified by Equation (5.6) will yield sufficiently accurate solutions. It is also worth noting that when multiple solutions within a frequency bandwidth are averaged, individual solutions with higher values of error will be smoothed out, and bandwidth averaged results can be considered generally at a higher level of accuracy.

5.2.5.3 Other effects

It was also found that for QRD designs with long slender wells ($d_{\max}/w > 6$), the solution was slower to converge and smaller element sizes may be needed. Cox & D'Antonio [7] suggest modelling QRDs with long thin wells with the BEM results in reduced accuracy, due to the absorption effects of the surface boundary layers that are not taken into account. For this reason, modelling QRDs with long thin wells will be largely avoided in this work.

5.2.6 Element size guidelines

From the above sections, the following guidelines for element size when modeling QRDs can be recommended:

1. The element size is smaller than 2.5 times than the width of any thin panels; and
2. The desired level of accuracy can be reached for element sizes smaller than that specified above, using the equation

$$e_{\max} = \frac{1}{\sqrt{20}} \sqrt{\frac{20\left(\frac{\mathrm{E}}{631}\right)^{\frac{2}{1.5}}}{\left(\frac{0.048}{{w_T}^2 {n_w}^2}\right) + \left(\frac{f}{c}\right)^2}}\,.$$

5.3 BEM code development and optimisation conclusion

The objective of Part II of this study was to further the work of Rocchi [23] and Smith [28] with a MATLAB implementation of the BEM. The primary aim was the optimisation of solution speed and accuracy, when used for diffusion modelling of Schroeder diffusers. The development of additional functionality was designed to increase the modelling capabilities of the code.

Chapter 5 outlines the changes made to the BEM code during this study. The capability to model a point source acoustic field, run multiple tests within frequency bandwidths and calculate the normalised diffusion coefficient is included. By intelligently discretising the geometry with reduced element size at corners, reduced number of elements are required for a desired level of accuracy. Numerous geometry creation functions allow for QRDs to be modelled easily, and also allow for geometric optimisation.

The speed and accuracy of the code is increased through a combination of computational technique and MATLAB algorithm improvements. An analytical solution for diagonal matrix terms is implemented, and the numerical integration method used is refined to prioritise the accuracy of element pairs within close proximity or on opposing sides of a corner. Code restructuring and re-writing allows for vectorised computations, and increases the computational efficiency. An average speed increase of approximately 50 times is recorded for models of varying diffuser sizes. The mentioned modifications, combined with the correction of minor errors in the original code, result in an average error of 200 times smaller when compared to an analytical solution.

Through convergence testing, an empirical relationship relating element size, frequency, geometry and error was derived. The BEM program is shown to be accurate to within $\pm 1\%$ with the capability to test most common Schroeder diffuser arrays across the required frequency band in under 3 hours. This implementation of the BEM can therefore be considered a useful tool in determining the detailed performance of Schroeder diffusers, and for the optimisation of their design.

5.3.1 Potential for further work

A number of further improvements are suggested to further increase the efficiency and functionality of the code, including:

- An implementation of the thin panel solution;
- Refinement of the number of Gaussian quadrature points used.
- A study into differences in modelling accuracy, if any, of acoustic fields with acute incident angles to the diffuser; and
- Compiling the MATLAB program into a lower level language for speed, and creating a graphical user interface to increase usability.

An opportunity was also recognised for the coupling of a full BEM and box model approach to numerical optimisation of Schroeder diffusers. By representing a Schroeder diffuser profile as a plane surface with varying complex surface impedance, the matrices [M] and [L] remain unchanged for models representing different well depths, and results can be obtained in a matter of seconds for different well depth arrangements [7]. The limitations of the box model, such as ignoring the effects of transverse wave propagation within wells, can be removed by testing diffuser designs of interest with a full BEM model. With the appropriate algorithms implemented, this may lead to the development of diffusers with superior performance compared to traditional Schroeder diffusers.

Part III

Investigation of Schroeder Diffuser Performance

Chapter 6

Investigation overview

With the use of the optimised and validated BEM from Part II, the performance of Schroeder diffusers can be modelled efficiently and with a known level of accuracy. The advantages of increased efficiency and accuracy are demonstrated, including the modelling of large and complex diffusers, for which limited published literature exists due to previous computation times involved.

6.1 Investigation scope and objectives

The investigation in Part III is limited to diffusion modelling of a source incident angle normal to the diffuser, or $\psi = 0$. This represents common diffuser applications, such as the rear wall of a performance space or monitoring studio, and walls of a room with a central source such as a musical rehearsal room. From the limitation of $\psi = 0$, this study does not provide information on second order reflection from walls and other surfaces that approach the diffuser at acute incident angles. However, these can be considered lesser in magnitude and importance, and Cox & D'Antonio state acoustic treatment is designed primarily to control first order reflections. c_d, c_r and c_p will therefore represent the diffusion, reference, and normalised diffusion coefficient for $\psi = 0$.

It is necessary to specify a similar total length when comparing the performance of multiple diffusers. For this reason, a total diffuser length of 2.4 m was chosen as a standard length during most tests in this study. This length represents many common applications of acoustic diffusers in small to medium spaces. There is no reason this study could not be repeated for a smaller or greater length if required.

This investigation seeks to determine the effects of:

1. prime number N, period length Nw_T, phase shifted sequences and incident acoustic field types on classical QRDs;

2. QRD fractal designs;

3. well divider thickness on Schroeder diffusers.

The normalised diffusion coefficient will be used as a data reduction tool in the comparison of polar diffusion patterns. A higher diffusion coefficient will be presumed to indicate a higher diffusion performance. However, the large amount of data lost in this simplification must be considered when interpreting results, and polar plot comparisons can be used for detailed comparisons.

6.2 Model details

The following parameters are used in models unless otherwise stated:

- The normalised diffusion coefficients c_n is calculated from (Eq. 2.2). Polar pressure distributions from 7 logarithmically spaced frequencies within one-third octave bands are averaged for each diffusion coefficient.

- QRD periods are modelled as an asymmetric sequence using (Eq. 2.6). Well divider panels are of thickness $0.1w$. Reference flat surfaces used when calculating c_r are rectangular prisms with width and thickness equal to the total width and thickness of the corresponding diffuser.

- The maximum element size for a discretised surface $e_{\max}$ is determined from (Eq. 5.6) with error less than $\pm 1\%$. Refined edge sizing is used (Chapter 5.1.4), with an edge-adjacent element size $e_{\text{edge}} = e_{\max}/3$, and number of inflation layers $n = 5$. The resultant element size factor for consecutive elements within the inflation region is 1.246.

- Each model calculates the pressure at 360 evenly spaced receivers along a 180° arc of radius 10 m from the diffuser centre. Where a point source is modelled, it is positioned directly in front of the diffuser centre at a distance of 5 m.

Chapter 7

Diffuser Performance Results and Discussion

This chapter provides a summary of each area of investigation, highlighting noteworthy results and discussing diffusers with particularly desirable or poor diffusion. Additional results are shown in Appendix A.

7.1 Performance of classical QRDs

The term classical QRD is used to represent a diffusers that strictly follows the quadratic residue sequence. Well established design equations for QRD geometry exist, derived from simplified theory that represent a QRD as a flat surface with varying complex surface impedance (Chapter 2.4.3). This theory is concerned with the prediction of diffusion lobes caused by phase grating reflections from varying well depths. From Chapter 2.4.3, the predicted lower frequency for diffusion lobes is the design frequency

$$f_0 = \frac{s_{\max} c}{2N d_{\max}} ,$$

and the upper frequency is

$$f_{\max} = \frac{1}{2w} .$$

There also exists a lower limit for diffusion lobes $f_{\min}$ dictated by the period width $Nw_{_T}$. However, an equation for this value is not specified in Schroeder's original paper [26] or the leading texts of Cox & D'Antonio [7] and Everest [11].

7.1.1 Effect of prime number N

The performance of QRD arrays with similar total length and varying N in a plane wave acoustic field is shown in Figure 7.1.1, and dimensions are listed in Appendix B.3. The high diffusion of QRDs with larger N is evident with respect to magnitude and bandwidth. Increases in bandwidth can be partially attributed to Nw_T, however diffusers with similar Nw_T such as $N = 11$ and $N = 17$ show differences in low frequency performance. This suggests that other factors, such as w or N, can affect low bandwidth response of QRDs. Significant diffusion begins at frequencies approximately between $\lambda < Nw_T < 2\lambda$ for most diffusers, and for QRDs with large N, significant diffusion occurs at over an octave below the design frequency f_0.

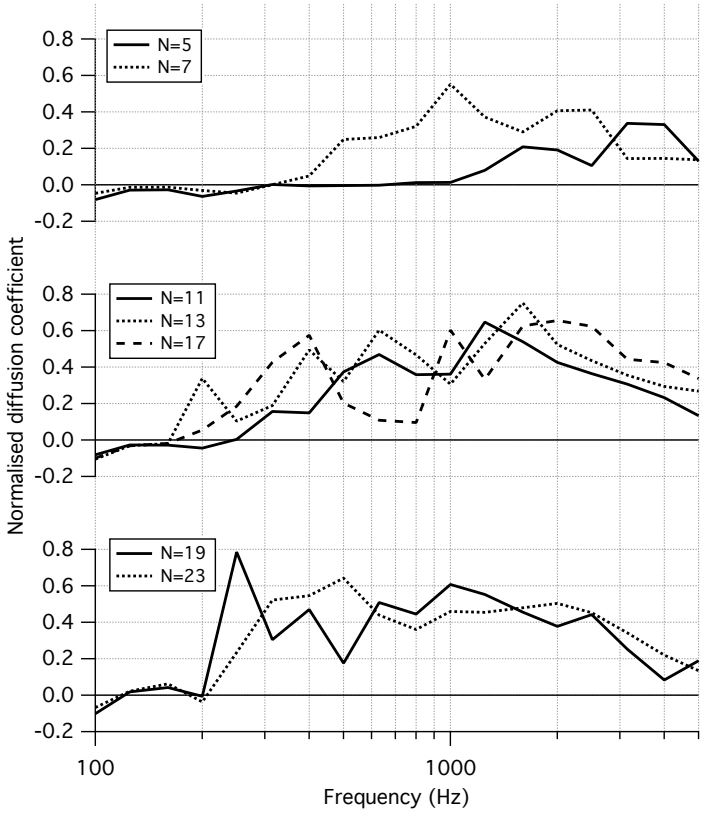

Figure 7.1.1: Performance of QRD arrays of total width 2.4 m, $f_0 =$ 500 Hz, and comparable well width w in a plane wave incident field. Diffuser dimensions listed in Appendix B.3.1.

7.1.2 Effect of acoustic field type

The same QRD arrays were tested in a point source acoustic field, two examples of which are shown in Figure 7.1.2. For $P > 1$, small changes in performance are observed. A general reduction in high frequency performance is explained by the increase in phase difference of the incident wave across the diffuser surface. For $P = 1$, large reductions in performance across most frequency bands are shown. Whether this is a result of the period width or the lack of repeating periods requires further testing to determine. However, the reduction in performance is so significant that the acoustic source location should be a major consideration when considering the effectiveness of large QRD sequences. Acoustic field comparisons for all QRDs from Figure 7.1.1 are shown in Appendix A.

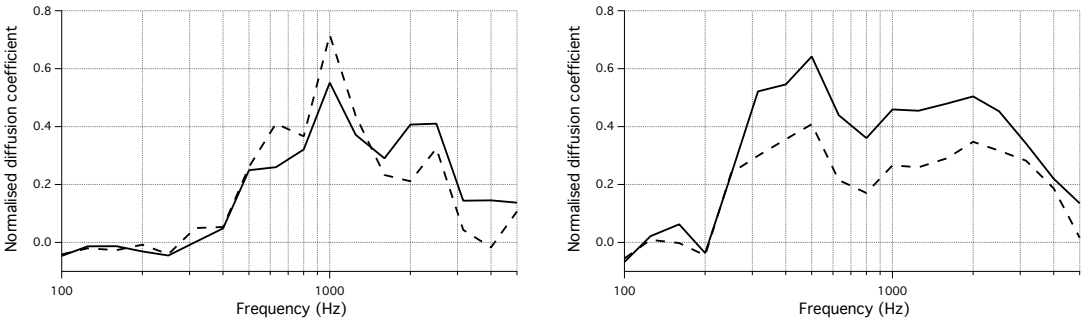

(a) $N = 7$, $P = 3$ (b) $N = 23$, $P = 1$

Plane wave - - - Point source 5 m from diffuser

Figure 7.1.2: Comparison of QRD performance in different acoustic fields. Total length 2.4 m, $f_0 = 500$ Hz.

7.1.3 Frequency range of diffusion for $N = 7$ QRDs

Shorter QRD sequences are the cheapest to build [7], which is perhaps why arguably the most commonly found QRD sequence is $N = 7$. The performance of $N = 7$ QRD arrays with similar total width and varying P is shown in Figure 7.1.3a. From this data, the upper and lower frequency limits for significant diffusion are displayed in Figure 7.1.3b and 7.1.3c respectively. Significant diffusion was defined as $c_n > 0.1$.

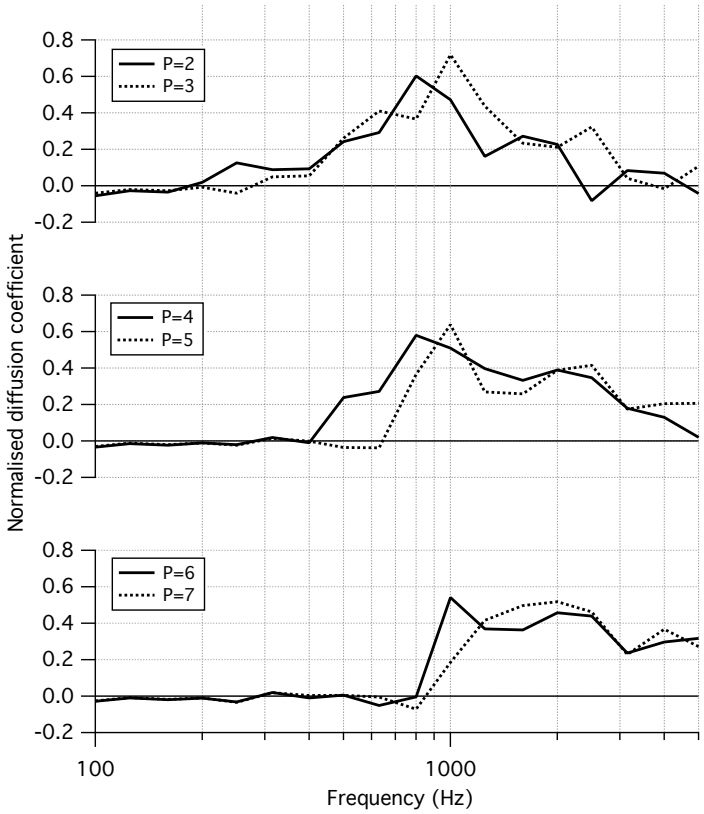

(a) Diffuser performance

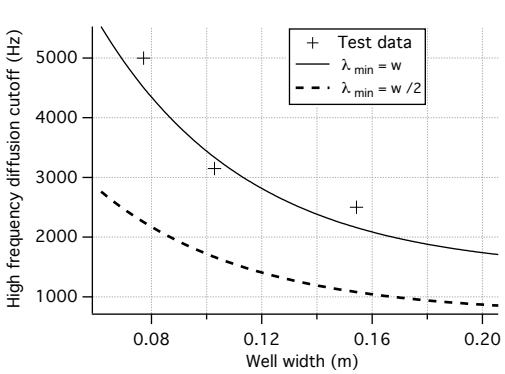

(b) High frequency cutoff

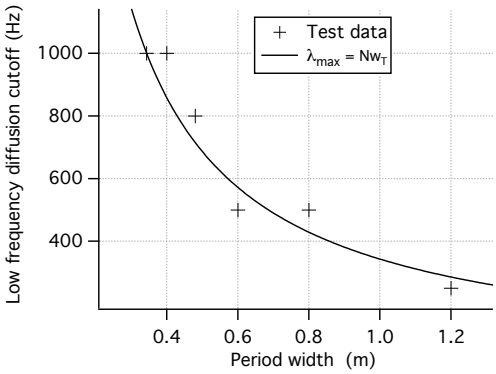

(c) Low frequency cutoff

Figure 7.1.3: Performance data for $N = 7$ QRD arrays with varying P. Total width 2.4 m, $f_0 = 500$ Hz, point source 5 m from the diffuser centre.

In Figure 7.1.3b a curve with a broken line shows the the upper frequency limit of Schroeder's predictions (Eq. 2.4). This results of this study show reduced but significant diffusion until approximately double this value, however this high frequency limit was reached in only three cases. No definitive conclusion can be drawn regarding an exact high frequency limit, but it is clear significant performance is possible past the upper limit of Schroeder's predictions.

In contrast, strong conclusions can be drawn from the lower frequency limit of $N = 7$ QRD performance, f_{low}. Figure 7.1.3c shows all data with the relationship $f_{\text{min}} \approx N w_T$, however more testing is required to confirm that this is not also a function of the design frequency f_0. The results of the previous test in Figure 7.1.1 suggest this relationship cannot be extended to QRDs with different N.

7.1.4 Effect of phase shifted sequences

Figure 7.1.4 shows a comparison of performance between a phase shifted QRD (see Chapter 2.4.4.2) and a classical QRD. The purpose of this comparison is to determine whether diffusion properties are consistent between the two sequences. It concludes that diffusion characteristics are varied between the two designs. The diffusion bandwidth of the phase shifted sequence is reduced, but shows increased performance consistency. Conclusions about the qualitative performance of this phase shifted sequence cannot be extended to other diffusers, but from this example it is reasonable to assume that phase shifted sequences may perform differently to regular sequences in most cases.

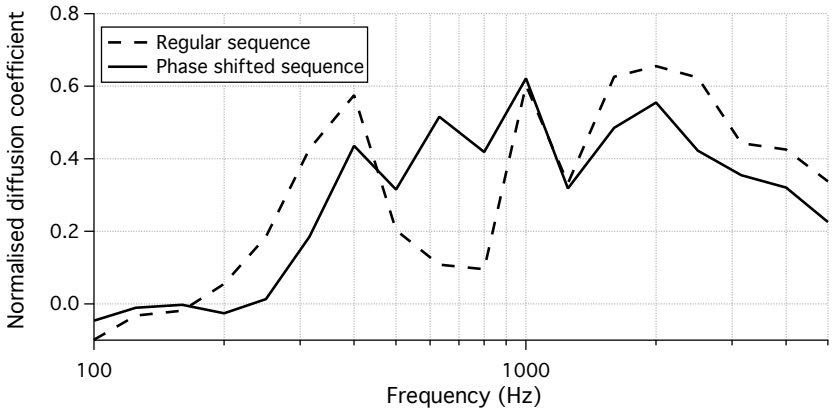

Figure 7.1.4: Comparison of regular and phase shifted QRD performance. $N = 13$, total width = 2.4, $P = 2$, $f_0 = 500$ Hz, $k = 4$.

7.2 QRD fractals

One of the greatest benefits offered by increased computation efficiency is the ability to model more complex geometry in detail. An example of this is the ability to model fractal diffuser designs. A limited amount of research has been done into numerical modelling of diffusion from two dimensional random fractal surfaces, such as that by Bradley et al. [5]. However, detailed modelling of complete fractal Schroeder diffusers with the BEM is not available in the public domain. Diffusion from a traditional fractal design, as well as from two novel designs are modelled in this study.

QRD fractal designs are implemented to extend the upper frequency limit of diffusion. As part of this study, three different fractal designs were tested in comparison to a reference QRD array. The fractal QRD designs, shown in Figure 7.2.1, are:

1. A symmetrical reference $N = 7$ QRD with total length 2.4 m, $P = 2$, and $f_0 = 400$ Hz. This is also used as the parent QRD for fractal designs;
2. a nested QRD with $(Nw_{_T})_{\text{frac}} = w$, and $f_{0,\text{frac}} = 1500$ Hz;
3. a nested convex quadratic curve with maximum height $w/2$; and
4. a nested concave quadratic curve with maximum height $w/2$.

The well depths of the reference QRD are adjusted slightly in each case, to account for the effective change in fractal QRD well depth due to the nested shape profile. The expected high frequency limit of the reference QRD, as calculated from results in Chapter 7.1, is approximately 2280 kHz. To compare high frequency performance, fractal designs and the reference QRD are tested over an extended frequency range up to 6300 Hz.

Results are displayed in Figure 7.2.2. The fractal QRD design shows very high performance, with consistently high diffusion properties extending beyond the high frequency limit of the reference QRD. The dimensions of the parent and nested QRD were chosen arbitrarily, and hence the diffusion properties will likely be further improved by an optimised fractal QRD design.

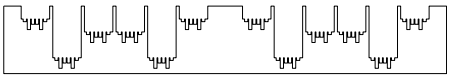

(a) Nested QRD

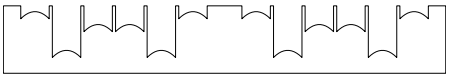

(b) Nested convex curve

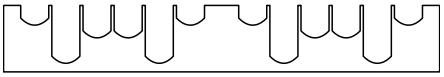

(c) Nested concave curve

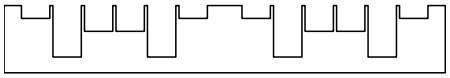

(d) Reference QRD

Figure 7.2.1: Four fractal-type QRD designs tested for diffusion frequency bandwidth.

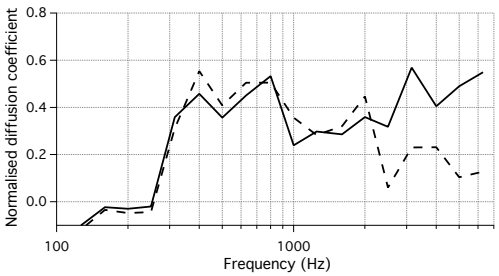

(a) Nested QRD

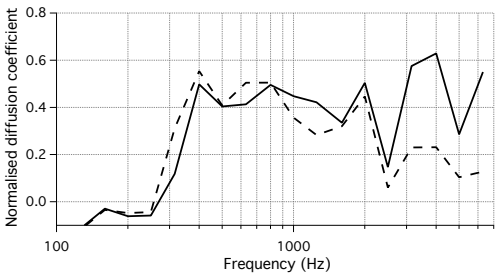

(b) Nested convex curve

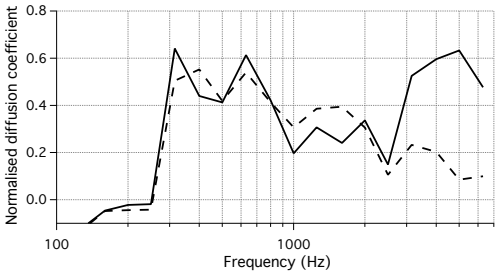

(c) Nested concave curve

Fractal design - - - Reference QRD

Figure 7.2.2: Comparison of three fractal designs and regular QRD performance. Parent $N = 7$ QRD, $Nw_T = 1.05$ m, $f_0 = 400$ Hz.

The convex and concave fractal diffusers both show increased performance above 3000 Hz. However, at 2500 Hz, poor performance is noted, with minimal increases when compared to the reference QRD. This frequency band is in close proximity to the critical frequency of the reference QRD $f_c = 2800$ Hz (see Chapter 2.4.3.2). The results suggests that, while providing large high frequency improvements, curved fractal designs may be ineffective at reducing the effect of specular reflections at critical frequencies.

When comparing the diffusion from nested QRD and curved surface fractals, it is important to consider the relative manufacturing cost for each design. Curved surfaces require relatively little additional cost and considerations. Conversely, nested QRDs require detailed construction with thin panels; if significant attention is not given to materials and construction method, significant absorption losses can arise from resonant vibration.

The preliminary tests of curved fractal QRD designs show that they are effective in extending the diffusion bandwidth of classical QRDs. Their performance is exceeded by a nested QRD fractal design, however their simplicity of design offers potential for a cost effective increase to the high frequency diffusion properties of classical QRDs. Further study of this design, including more repeating periods and testing at incident angles, is needed to confirm these findings. Optimisation of the curve profile is likely to increase their performance.

7.3 Well divider panel thickness

The thickness, w_P, and stiffness of well diving panels is an important design consideration of Schroeder diffusers. As discussed, they must act as rigid reflectors to minimise absorption, while at the same time be as thin as possible to maximise the effect of the phase grating design of Schroeder diffusers [7]. A balance must therefore be found between high stiffness and reflective properties, and minimal thickness.

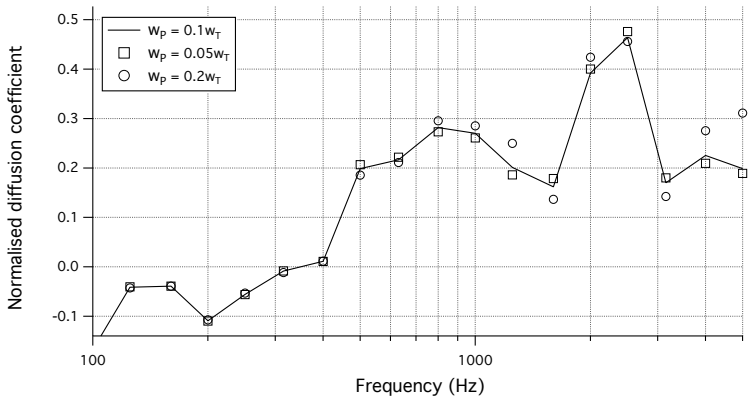

Figure 7.3.1: Effect of thin panel width on diffuser performance. $N = 7$ QRD, total width = 2.4 m, $P = 4$, $f_0 = 500$ Hz.

Varying panel thicknesses were tested to determine whether they resulted in significant differences in diffusion performance. This information can be used not only in the design of Schroeder diffusers, but also in determining for which frequencies the thin panel solution is an appropriate method of modelling.

Figure 7.3.1 shows the diffusion performance of a typical $N = 7$ QRD array. The solid line indicates a thin panel width of $w_P = 0.1w_T$ used throughout this work, and markers represent performance with panel widths of half and double this value. For frequencies below 500 Hz, differences are minimal and are smaller than the estimated error bounds of the BEM solution. Between 500 Hz and 3000 Hz, differences are noted as considerably larger than the estimated accuracy of the BEM solution, however not notably different for the purpose of evaluating the performance of the diffuser. Above 3000 Hz, significant differences arise, in particular with a larger panel width.

Interestingly, the larger panel width results in a higher diffusion coefficient for frequencies above 3000 Hz. An explanation may be that reflections from panel tips provide omni-directional scattering similar to a flat plate at low frequencies, which is likely only to occur only for incident angles of $\psi = 0°$. This finding may also be a result of the incident acoustic field type, in this case a point source field. An analysis of the polar diffusion patterns would aid in determining, in this instance, whether larger panel widths do in fact provide superior diffusion, or whether it is misleading to reduce a large amount of data by representing a polar plot with a single coefficient. Further testing is required to extend this finding to other diffusers and acoustic field types.

From the results discussed above, it is concluded that for frequencies below 500 Hz, differences in performance due to panel width within $0.05 - 0.2w_T$ are not noticeable, and the thin panel solution is an appropriate method of analysis. Between 500 Hz and 3000 Hz, the thin panel solution may be appropriate when high accuracy is not required. However, above 3000 Hz, a full BEM model is necessary to evaluate the diffusion performance.

Chapter 8

Conclusion and key findings

The objective of Part III was to determine the effect of different parameters on the performance of Schroeder diffusers. The diffuser sizes considered are suitable for small-medium diffuser applications, with a diffuser length not exceeding 2.4 m. The advantages derived from the development of a BEM code with increased efficiency and accuracy were demonstrated, in particular for modelling complex geometry of multiple periods. A systematic approach was taken to modelling the performance of classical QRDs with varying parameters. In preliminary tests, the high performance of two novel diffuser designs is an exciting design development.

The key findings from the investigation are summarised as:

- Classical QRD arrays with larger N were confirmed to display superior diffusion in a plane wave acoustic field.
- Diffusion from single period QRD arrays with large period length reduced significantly in a point source acoustic field, when compared to a plane wave field. Diffusers of multiple periods and smaller period lengths performed similarly in both fields.
- The effective diffusion bandwidth of the common $N = 7$ QRD array can be estimated with reasonable accuracy from the diffuser geometry.
- QRD fractal arrays with nested QRDs are confirmed to be a very effective method for extending the high frequency diffusion performance of classical QRDs. Preliminary tests of fractal QRD arrays with nested convex and concave curves show strong potential for comparable increases in high frequency diffusion with considerably simpler construction.
- The thin panel solution is an appropriate method for modelling Schroeder diffusers below 3000 Hz, in particular below 500 Hz. However, above 3000 Hz, differences

caused by thin panel thickness are significant and a full BEM model is required.

8.0.1 Potential for further work

While some results from this work serve to confirm the findings of others, multiple avenues for further research into diffusers are suggested, including:

- Comparing solutions derived using with the thin panel solution BEM to those using the regular BEM;
- The effect of acute incident angles on the performance of classical QRD arrays;
- Confirmation of the strong high frequency performance of nested convex and concave fractal QRD arrays, including the effect of larger arrays, incident angle and curve equation on diffusion performance; and
- Experimental measurement of diffusion and absorption properties of fractal designs, to validate model results and quantify the absorption losses from high frequency diffusion within deep wells.

Bibliography

[1] Planning guide for performance spaces. `http://www.wengercorp.com`, 2008.

[2] ISO 17497-1:2004. Acoustics - sound-scattering properties opf surfaces. part 1: Measurement of the random-incidence scattering coefficient in a reverberation room. 2004.

[3] AES 4is 2001 (r2007). Information document for room acoustics and sound reinforcement systems - characterisation and measurement of surface scattering uniformity. *J. Audio Eng. Soc*, 49(3):149–65, 2001.

[4] Milton Abramowitz and Irene A Stegun. *Handbook of mathematical functions: with formulas, graphs, and mathematical tables*. Number 55. Courier Dover Publications, 1972.

[5] David Bradley, Erik O Snow, Kimberly A Riegel, Zachary D Nasipak, and Andrew S Terenzi. Numerical prediction of sound scattering from surfaces with fractal geometry: A preliminary investigation. In *Proceedings of Meetings on Acoustics*, volume 12, page 015010. Acoustical Society of America, 2014.

[6] TJ Cox. Acoustic diffusers: the good, the bad and the ugly. *Proceedings of the Institute of Acoustics.*, 20, 2005.

[7] Trevor J Cox and Peter D'antonio. *Acoustic absorbers and diffusers: theory, design and application*. CRC Press, 2009.

[8] Trevor J Cox and YW Lam. Prediction and evaluation of the scattering from quadratic residue diffusers. *The Journal of the Acoustical Society of America*, 95(1):297–305, 1994.

[9] Peter D'Antonio and John Konnert. The QRD diffractal: a new one- or two-dimensional fractal sound diffusor. *Journal of the Audio Engineering Society*, 40(3):117–129, 1992.

[10] RPG Diffusor Systems Inc. QRD® 734. `http://www.rpginc.com/product_QRD734.cfm`, October 2014.

[11] Ken C. Pohlmann F. Alton Everest. *Master Handbook of Acoustics*. McGraw-Hill, 2009.

[12] Pingzhi Fan and Michael Darnell. *Sequence design for communications applications*, volume 30. Research Studies Press Taunton, 1996.

[13] Dennis Fleigher. Technical note: FYI re RPGs & QRDs, 1990.

[14] K Fujiwara. A study on the sound absorption of a quadratic-residue type diffuser. *Acta Acustica united with Acustica*, 81(4):370–378, 1995.

[15] K Fujiwara and T Miyajima. Absorption characteristics of a practically constructed shroeder diffuser of quadratic-residue type. *Applied Acoustics*, 35(2):149–152, 1992.

[16] RPG Diffusor Systems Inc. QRD 734 random incidence performance data. `http://rpginc.com/product_QRD734.cfm`, October 2014.

[17] Stephen Kirkup. *The boundary element method in acoustics*, volume 129. Integrated sound software Heptonstall, 1998.

[18] Erwin Kreyszig. *Advanced engineering mathematics*. John Wiley & Sons, 2007.

[19] Tamio Kuyama. Some calculated results of the diffraction of sound waves by a cylindrical obstacle. *The Naval Experimental and Research Establishment.*, 1933.

[20] MathWorks. Techniques for improving performance (MATLAB). `http://www.mathworks.com.au/help/matlab/matlab_prog/techniques-for-improving-performance.html`, May 2014.

[21] Philip M. Morse. *Theoretical Acoustics*. Princeton University Press, 1986.

[22] J. H. Rindel. Attenuation of sound reflections from curved surfaces. Proc. 25th Conference on Acoustics, 1985.

[23] Luca Rocchi. Quadratic residue diffusers: Modelling through the boundary element method. *Bachelor of Engineering with Honours thesis, UTAS.*

[24] Harry A Schenck. Improved integral formulation for acoustic radiation problems. *The journal of the acoustical society of America*, 44(1):41–58, 1968.

[25] Manfred R Schrdder. Diffuse sound reflection by maximum- length sequences. *The Journal of the Acoustical Society of America*, 57(1):149–150, 1975.

[26] Manfred R Schroeder. Binaural dissimilarity and optimum ceilings for concert halls: More lateral sound diffusion. *The Journal of the Acoustical Society of America*, 65(4):958–963, 1979.

[27] AF Seybert and TK Rengarajan. The use of CHIEF to obtain unique solutions for acoustic radiation using boundary integral equations. *The journal of the acoustical society of America*, 81(5):1299–1306, 1987.

[28] Nicholas Smith. Acoustic diffusion: Simulation and analysis through the boundary element method and finite element method. *Bachelor of Engineering with Honours thesis, UTAS.*

[29] T Terai. On calculation of sound fields around three dimensional objects by integral equation methods. *Journal of Sound and Vibration*, 69(1):71–100, 1980.

[30] Peter D'Antonio Trevor J. Cox. Thirty years since "diffuse sound reflection by maximum-length sequences": Where are we now? *Forum Acusticum*, 2005.

[31] Francis M Wiener. Sound diffraction by rigid spheres and circular cylinders. *The Journal of the Acoustical Society of America*, 19(3):444–451, 1947.

[32] TW Wu. A direct boundary element method for acoustic radiation and scattering from mixed regular and thin bodies. *The Journal of the Acoustical Society of America*, 97(1):84–91, 1995.

Appendix A

Additional results

A.1 QRD performance results

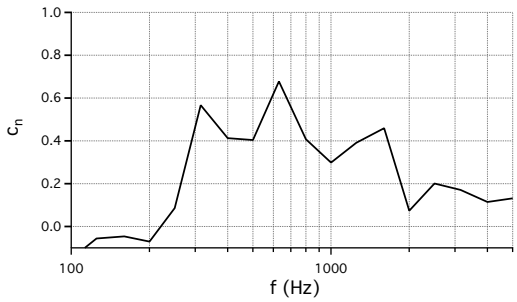

(A.1) $N = 7$, $f_0 = 300$ Hz, $P = 2$

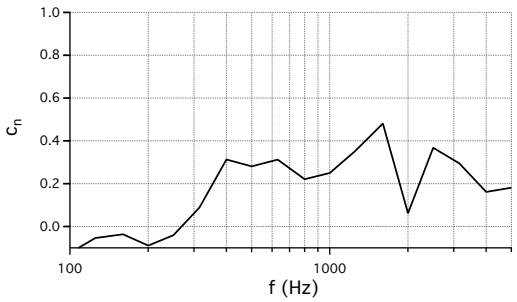

(A.2) $N = 7$, $f_0 = 300$ Hz, $P = 3$

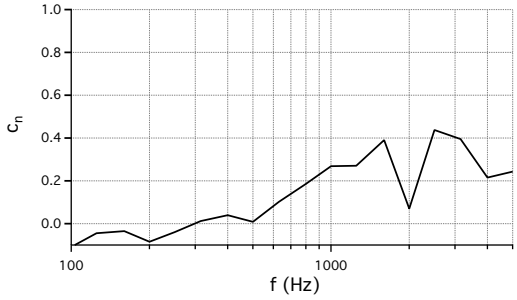

(A.3) $N = 7$, $f_0 = 300$ Hz, $P = 4$

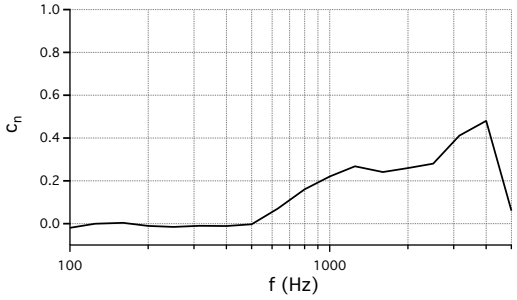

(A.4) $N = 7$, $f_0 = 300$ Hz, $P = 5$

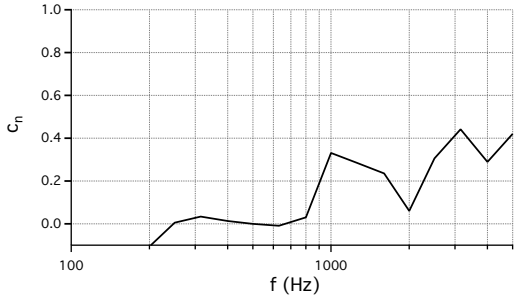

(A.5) $N = 7$, $f_0 = 300$ Hz, $P = 6$

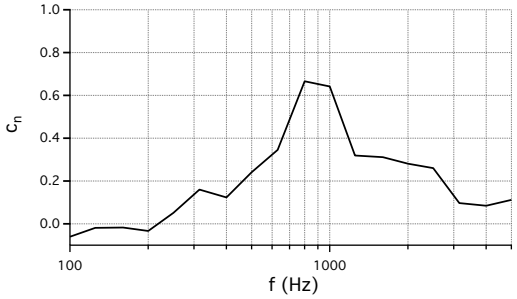

(A.6) $N = 7$, $f_0 = 500$ Hz, $P = 2$

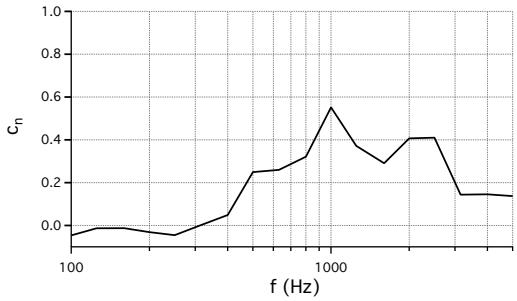

(A.7) $N = 7$, $f_0 = 500$ Hz, $P = 3$

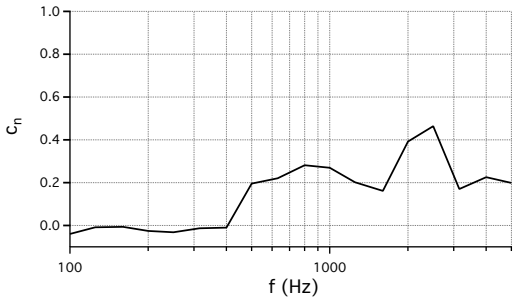

(A.8) $N = 7$, $f_0 = 500$ Hz, $P = 4$

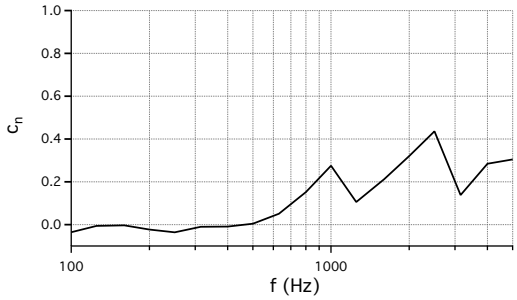

(A.9) $N = 7$, $f_0 = 500$ Hz, $P = 5$

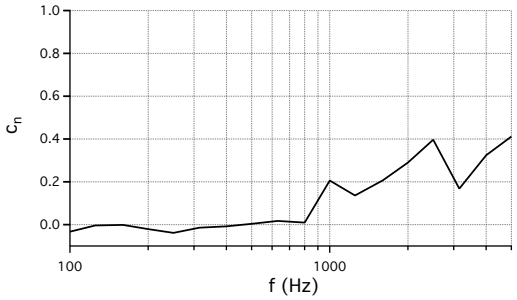

(A.10) $N = 7$, $f_0 = 500$ Hz, $P = 6$

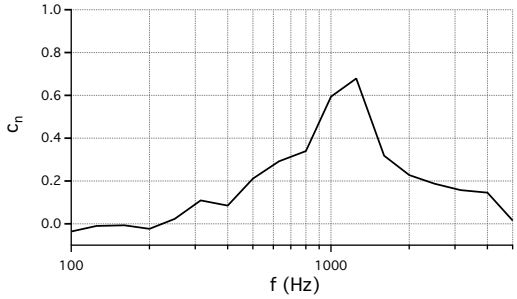

(A.11) $N = 7$, $f_0 = 700$ Hz, $P = 2$

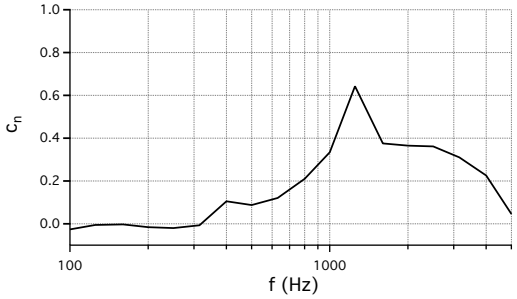

(A.12) $N = 7$, $f_0 = 700$ Hz, $P = 3$

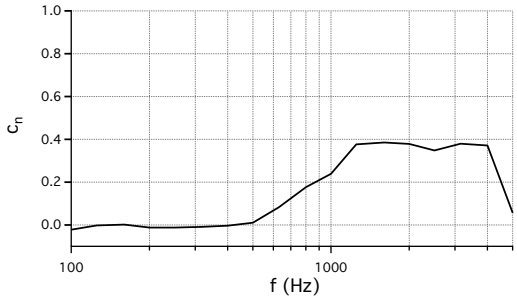

(A.13) $N = 7$, $f_0 = 700$ Hz, $P = 4$

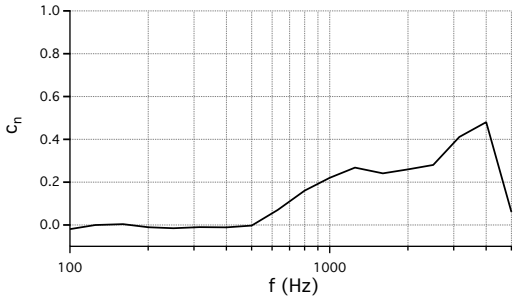

(A.14) $N = 7$, $f_0 = 700$ Hz, $P = 5$

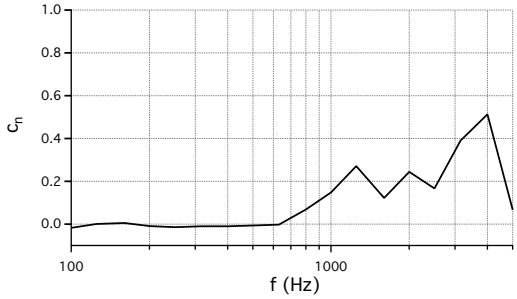

(A.15) $N = 7$, $f_0 = 700$ Hz, $P = 6$

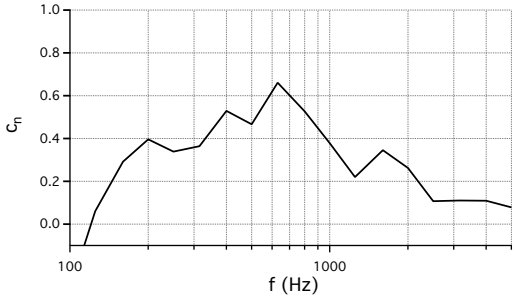

(A.16) $N = 11$, $f_0 = 300$ Hz, $P = 1$

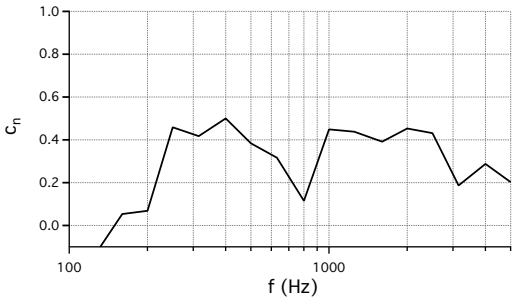

(A.17) $N = 11$, $f_0 = 300$ Hz, $P = 2$

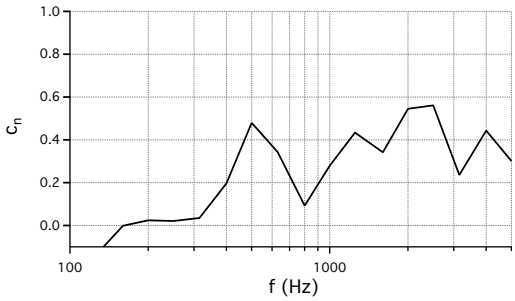

(A.18) $N = 11$, $f_0 = 300$ Hz, $P = 3$

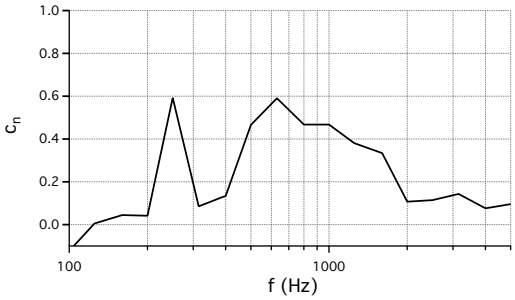

(A.19) $N = 11$, $f_0 = 500$ Hz, $P = 1$

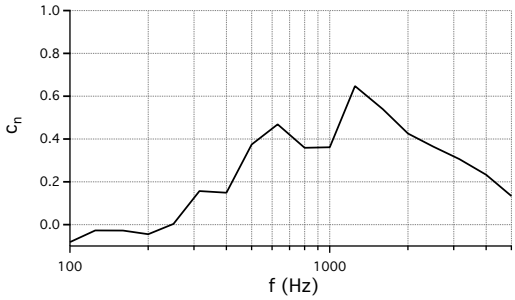

(A.20) $N = 11$, $f_0 = 500$ Hz, $P = 2$

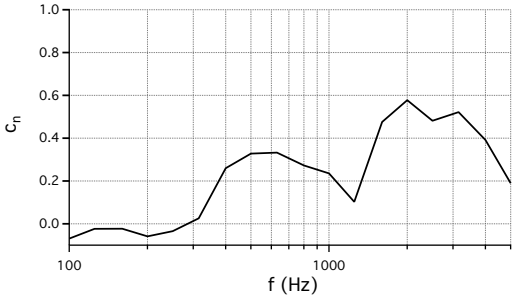

(A.21) $N = 11$, $f_0 = 500$ Hz, $P = 3$

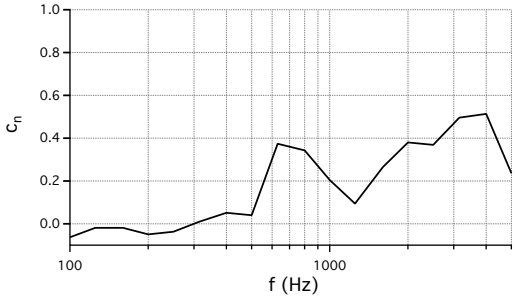

(A.22) $N = 11$, $f_0 = 500$ Hz, $P = 4$

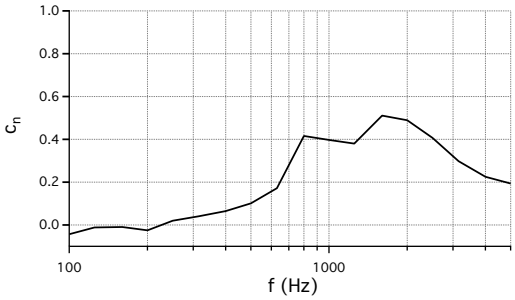

(A.23) $N = 11$, $f_0 = 700$ Hz, $P = 2$

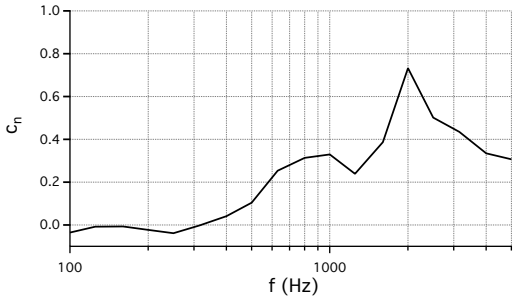

(A.24) $N = 11$, $f_0 = 700$ Hz, $P = 3$

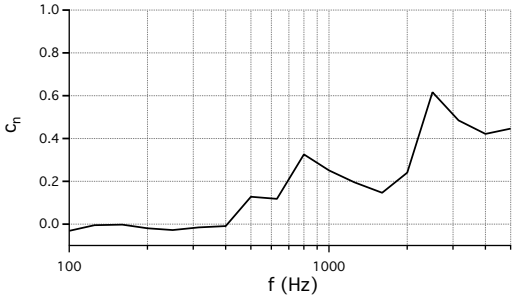

(A.25) $N = 11$, $f_0 = 700$ Hz, $P = 4$

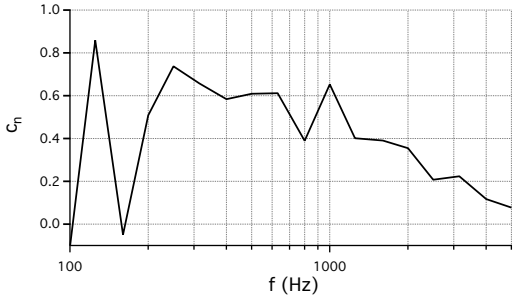

(A.26) $N = 13$, $f_0 = 300$ Hz, $P = 2$

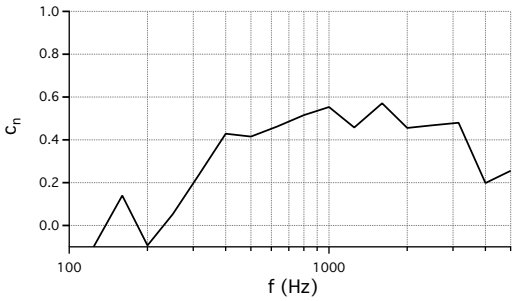

(A.27) $N = 13,\ f_0 = 300$ Hz, $P = 3$

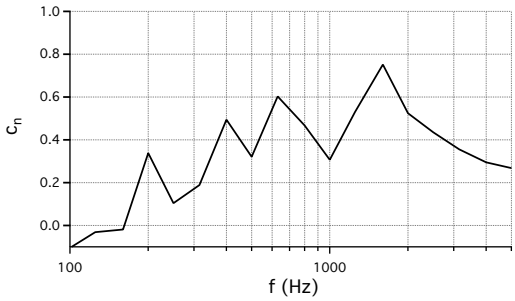

(A.28) $N = 13,\ f_0 = 500$ Hz, $P = 2$

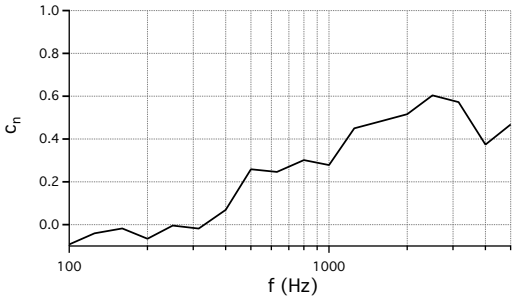

(A.29) $N = 13,\ f_0 = 500$ Hz, $P = 3$

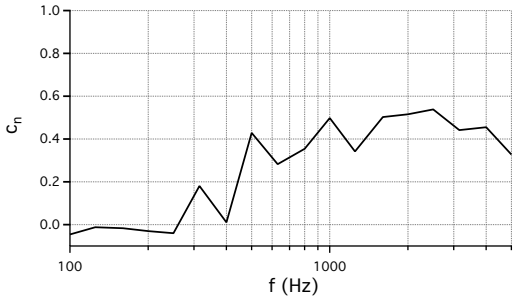

(A.30) $N = 13,\ f_0 = 700$ Hz, $P = 3$

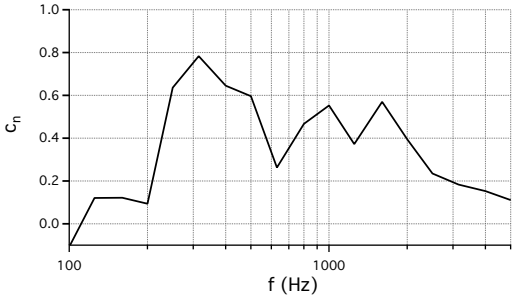

(A.31) $N = 17,\ f_0 = 500$ Hz, $P = 1$

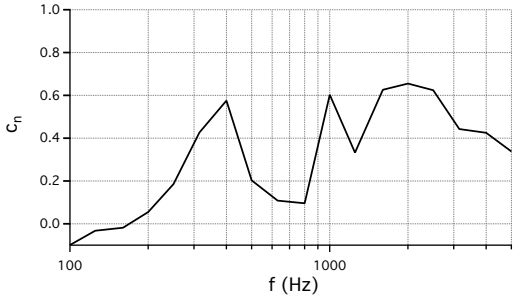

(A.32) $N = 17,\ f_0 = 500$ Hz, $P = 2$

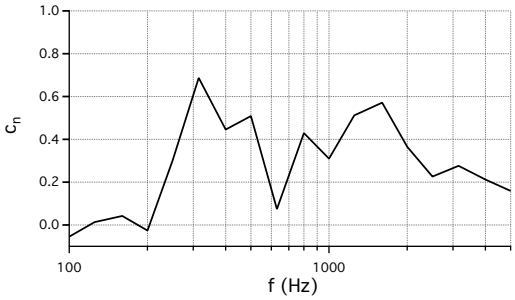

(A.33) $N = 17,\ f_0 = 700$ Hz, $P = 1$

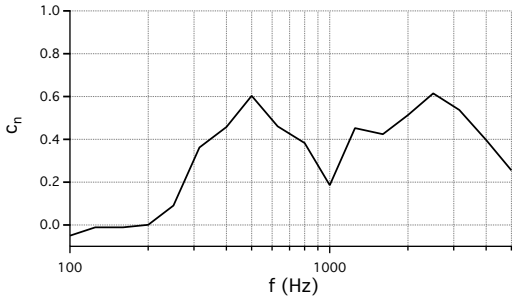

(A.34) $N = 17,\ f_0 = 700$ Hz, $P = 2$

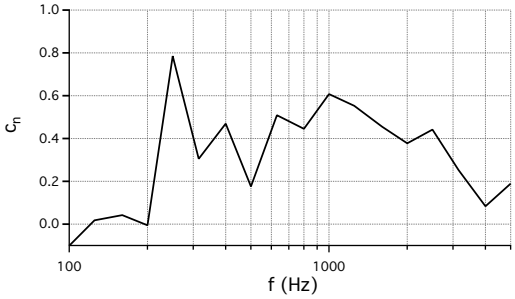

(A.35) $N = 19,\ f_0 = 500$ Hz, $P = 1$

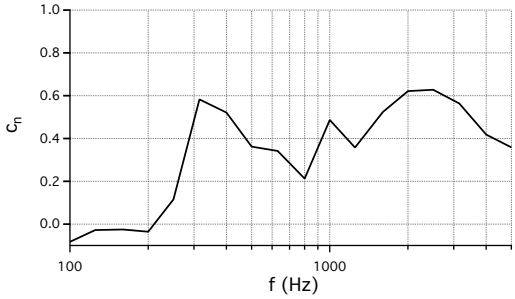

(A.36) $N = 19,\ f_0 = 500$ Hz, $P = 2$

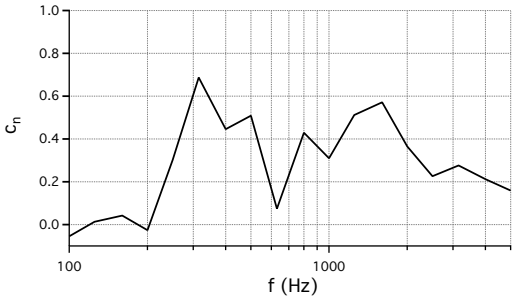

(A.37) $N = 19$, $f_0 = 700$ Hz, $P = 1$

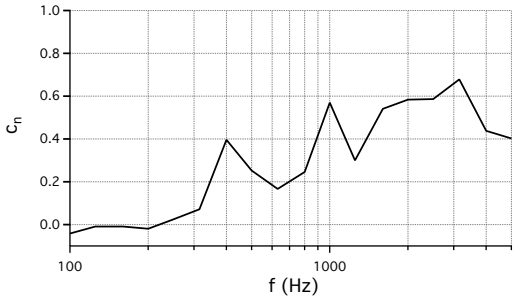

(A.38) $N = 19$, $f_0 = 700$ Hz, $P = 2$

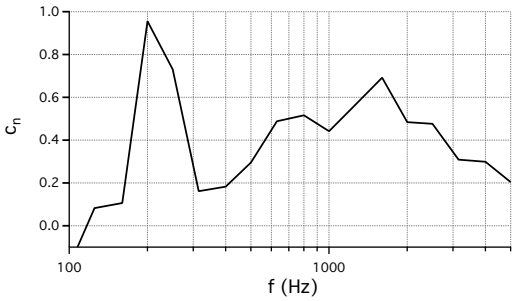

(A.39) $N = 23$, $f_0 = 300$ Hz, $P = 1$

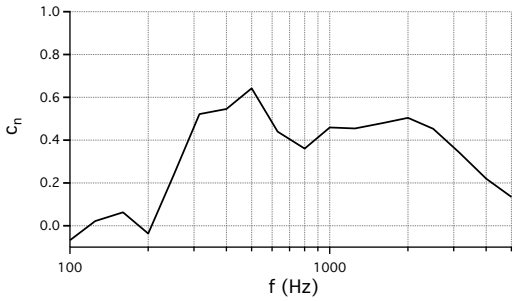

(A.40) $N = 23$, $f_0 = 500$ Hz, $P = 1$

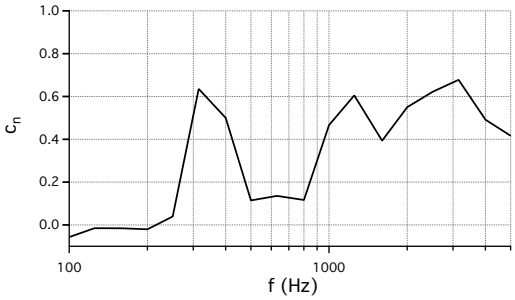

(A.41) $N = 23$, $f_0 = 500$ Hz, $P = 2$

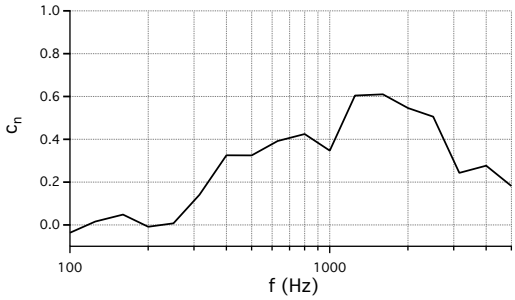

(A.42) $N = 23$, $f_0 = 700$ Hz, $P = 1$

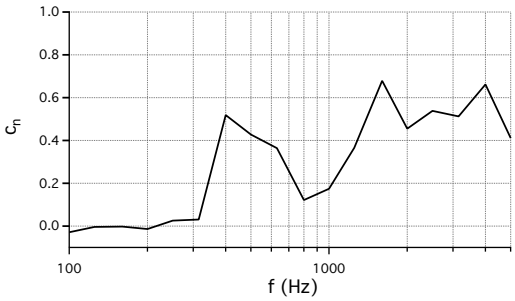

(A.43) $N = 23$, $f_0 = 700$ Hz, $P = 2$

Figure A.1.1: QRD diffusion data. Total array length of 2.4 m, plane wave acoustic field, $\psi = 0°$.

A.2 Acoustic field comparison results

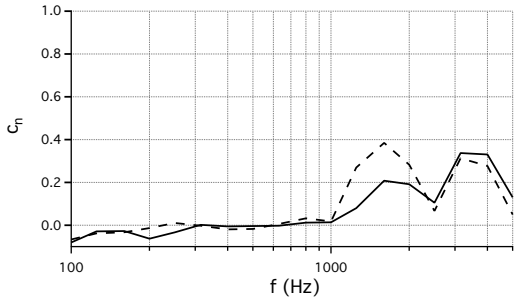

(A.1) $N = 5$, $P = 5$

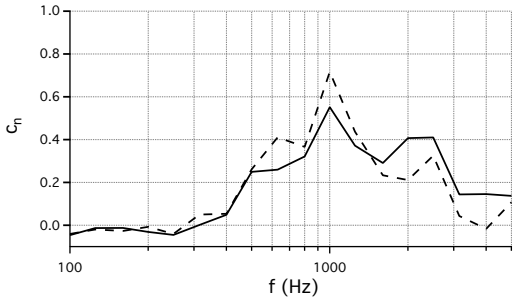

(A.2) $N = 7$, $P = 3$

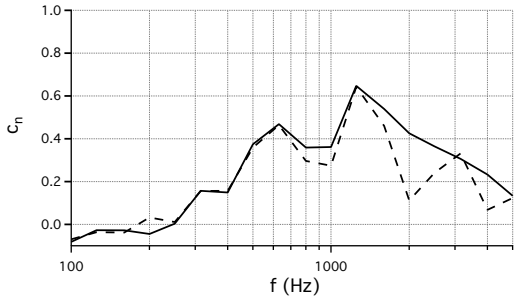

(A.3) $N = 11$, $P = 2$

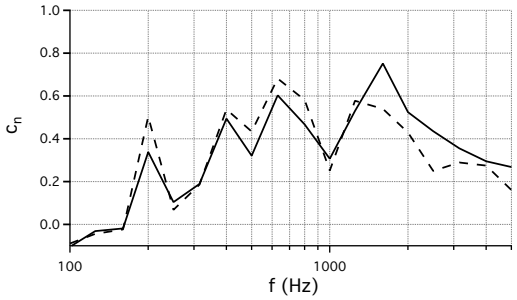

(A.4) $N = 13$, $P = 2$

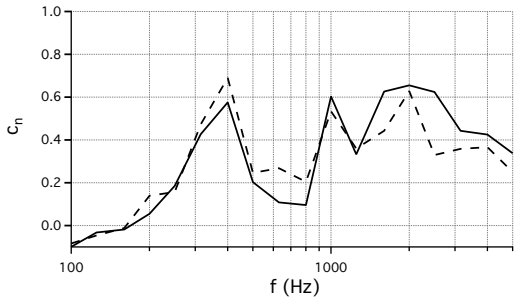

(A.5) $N = 17$, $P = 2$

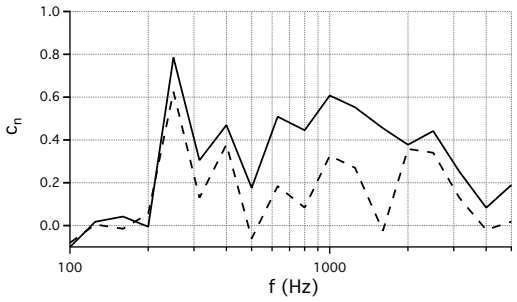

(A.6) $N = 19$, $P = 1$

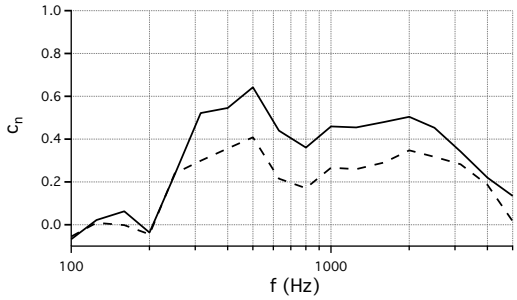

(A.7) $N = 23$, $P = 1$

Plane wave - - - Point source 5 m from diffuser

Figure A.2.1: Comparison of different acoustic fields for QRDs of comparable w and varying Nw_T. $f_0 = 500$ Hz. $\psi = 0°$

Appendix B

Additional details

B.1 BEM Program Steps

Table B.1.1: BEM program steps

Step	Type	Description	Ref.	Eq. #
1	**Input**	Diffuser geometry as a set of corner points and maximum element length.	Sect: 4.6	
2	**Input**	Incident sound field type, frequency, magnitude and incident angle.	Sect: 4.3	(4.7),(4.6)
3	**Input**	Set of off-surface receivers for evaluation.		
4	**Calculation**	Diffuser geometry discretised into set of elements.	Sect: 4.6, 5.1.4	
5	**Calculation**	Boundary condition solved for all elements.	Sect: 4.4	(4.8)
6	**Calculation**	Coefficient matrices [M] and [L] constructed for on-surface pressures.	Sect: 4.6, 4.8	(4.25),(4.26), (4.29)
7	**Calculation**	Matrix equation solved for potential values on surface.	Sect: 4.6	(4.15)
8	**Calculation**	Coefficient matrices [M] and [L] constructed for receiver pressures.	Sect: 4.6, 4.8	(4.25),(4.26), (4.29)
9	**Calculation**	Matrix equation solved for potential values at off-surface points.	Sect: 4.6	(4.14)
10	**Calculation**	Absolute value sound pressure calculated from acoustic potential and normalised.	Sect: 4.2	(4.2)
10	**Calculation/ output**	Diffusion coefficient calculated	Sect: 2.3.3.1	(2.1)
12	**Output**	Polar plot of diffracted pressure at receivers and total pressure at receivers.		
13	**(Optional)**	If normalised diffusion coefficient is required, processes 1-12 are repeated for a flat plate of similar dimensions to diffuser.	Sect: 2.3.3.1	(2.2)

B.2 A concise derivation of Green's second identity from the divergence theorem

From the previous definitions of $\phi(\boldsymbol{p})$ (Eq. 2.2) and $G(\boldsymbol{p}, \boldsymbol{q})$ (Eq. 4.5), both functions describe a sound field and therefore they must also satisfy the Helmholtz equation (Eq. 4.1) in their relevant domains. ϕ is defined everywhere within the domain, thus

$$\nabla^2\phi + k^2\phi = 0 \qquad\qquad \boldsymbol{p} \in V\,, \tag{B.1}$$

and $G(\boldsymbol{p}, \boldsymbol{q})$ is defined at at all points within the domain except at $\boldsymbol{q}$,

$$\nabla^2 G + k^2 G = 0 \qquad\qquad \boldsymbol{p} \in V,\, \boldsymbol{p} \neq \boldsymbol{q}\,. \tag{B.2}$$

From the divergence theorem

$$\iiint_V (\boldsymbol{\nabla} \cdot \boldsymbol{F})\mathrm{d}V = \oiint (\boldsymbol{F} \cdot \boldsymbol{n})\mathrm{d}S\,, \tag{B.3}$$

and the substitution of $(\boldsymbol{F} = \phi\,\nabla G - G\,\nabla\phi)$ results in

$$\iiint_V \phi(\,\nabla^2 G - G\,\nabla^2)\mathrm{d}V = \oiint \left(\phi\frac{\partial G}{\partial \hat{n}} - G\frac{\partial \phi}{\partial n}\right)\mathrm{d}S\,. \tag{B.4}$$

From (Eq.B.1) and (Eq.B.2), $\nabla^2 G$ and $\nabla^2\phi$ can be substituted to obtain

$$-\,k^2 \iiint_V (\phi\, G - G\,\phi)\mathrm{d}V = \oiint \left(\phi\frac{\partial G}{\partial n} - G\frac{\partial \phi}{\partial n}\right)\mathrm{d}S\,. \tag{B.5}$$

A modified domain can be represented as

$$V_m = V_o - V_q\,, \tag{B.6}$$

where V_m is the modified domain that excludes the point $\boldsymbol{q}$, V_o is the original domain, and V_q is an infinitesimal sphere surrounding the point $\boldsymbol{q}$. In the domain

V_m, $(\phi\, G - G\, \phi) = 0$. From this, combined with (Eq. B.6) and (Eq. B.5),

$$\oiint_{S_o} \left(\phi \frac{\partial G}{\partial n} - G \frac{\partial \phi}{\partial n} \right) \mathrm{d}S = - \oiint_{S_q} \left(\phi \frac{\partial G}{\partial n} - G \frac{\partial \phi}{\partial n} \right) \mathrm{d}S \,. \tag{B.7}$$

The surface of the sphere V_q can be represented by S_q, and the surface of the original domain V_o represented by S_o. As the radius of $S_q \to 0$, and assuming the function ϕ is smooth,

$$\phi \to \phi_q = \phi(\boldsymbol{q}) \,,$$

$$\nabla \phi_{S_q} \to \text{constant}$$

as S_q is a sphere, thus

$$\oiint_{S_q} \frac{\partial \phi}{\partial n} \mathrm{d}S = 0 \,.$$

For a sphere around a point source,

$$G = \text{constant} \,,$$

$$\frac{\partial G}{\partial n} = \frac{\partial G}{\partial r} = \text{constant} \,.$$

Using these identities, (Eq. B.7) becomes

$$\oiint_{S_o} \left(\phi \frac{\partial G}{\partial n} - G \frac{\partial \phi}{\partial n} \right) \mathrm{d}S = -\phi_q \frac{\mathrm{d}G}{\mathrm{d}r} A, \tag{B.8}$$

where A is the area of S_q at radius r. In two-dimensions where S_q represents a circle, this can be represented by the length of the circumference

$$A = 2\pi r \,. \tag{B.9}$$

The leading term in $\frac{\mathrm{d}G}{\mathrm{d}r}$ is inversely proportional to r, and therefore the right hand side of (Eq B.8) can be represented as

$$\oiint_{S_o} \left(\phi \frac{\partial G}{\partial n} - G \frac{\partial \phi}{\partial n} \right) \mathrm{d}S = -C\phi_q, \tag{B.10}$$

where C is a constant. Any arbitrary value of 1 is chosen for C, and G is scaled appropriately. While this describes the acoustic potential of $\boldsymbol{q}$, while $\boldsymbol{q}$ is within the domain V, it is not valid at the surface S_o which is on the border of the domain. From knowledge of the boundary conditions, this is where the BEM is solved. For a value of C at this boundary, an average is taken of the values for C when $\boldsymbol{q} \in V$ $(C = 1)$, and $\boldsymbol{q} \notin V$ $(C = 0)$, and therefore $C = 1/2$ for $\boldsymbol{q} \in S$.

From the value of $C = 1$ chosen, the appropriate scaling factor for the function G can be determined, using

$$\frac{\mathrm{d}G(\boldsymbol{q})}{\mathrm{d}r} = \frac{1}{2\pi r}, \quad r \to 0 \tag{B.11}$$

for two-dimensional problems.

B.3 Diffuser dimensions

N	P (m)	$Nw_{_T}$ (m)
5	5	0.48
7	3	0.8
11	2	1.2
13	2	1.2
17	2	1.2
19	1	2.4
23	1	2.4

Table B.3.1: Table of QRD dimensions for test as shown in Figure 7.1.1

B.4 Specifications of Computer used in code timing

Table B.4.1: Specifications of computer used in code timing

Type	Macintosh MacBook Pro
Processor	2.3 GHz quad-core i7
RAM	16 GB
MATLAB version	2013a Student version

B.5 Gaussian quadrature weights and abscissae

The Gaussian quadrature data used is published by Abramowitz & Stegun [4].

Table B.5.1: Gaussian Quadrature data for $n = 2$

w_i	x_i
1.0000000000000000	-0.5773502691896257
1.0000000000000000	0.5773502691896257

Gaussian Quadrature data for $n = 4$

w_i	x_i
0.6521451548625461	-0.3399810435848563
0.6521451548625461	0.3399810435848563
0.3478548451374538	-0.8611363115940526
0.3478548451374538	0.8611363115940526

Gaussian Quadrature data for $n = 6$

w_i	x_i
0.3607615730481386	0.6612093864662645
0.3607615730481386	-0.6612093864662645
0.4679139345726910	-0.2386191860831969
0.4679139345726910	0.2386191860831969
0.1713244923791704	-0.9324695142031521
0.1713244923791704	0.9324695142031521

Gaussian Quadrature data for $n = 10$

w_i	x_i
0.2955242247147529	-0.1488743389816312
0.2955242247147529	0.1488743389816312
0.2692667193099963	-0.4333953941292472
0.2692667193099963	0.4333953941292472
0.2190863625159820	-0.6794095682990244
0.2190863625159820	0.6794095682990244
0.1494513491505806	-0.8650633666889845
0.1494513491505806	0.8650633666889845
0.0666713443086881	-0.9739065285171717
0.0666713443086881	0.9739065285171717

Gaussian Quadrature data for $n = 20$

w_i	x_i
0.1527533871307258	-0.0765265211334973
0.1527533871307258	0.0765265211334973
0.1491729864726037	-0.2277858511416451
0.1491729864726037	0.2277858511416451
0.1420961093183820	-0.3737060887154195
0.1420961093183820	0.3737060887154195
0.1316886384491766	-0.5108670019508271
0.1316886384491766	0.5108670019508271
0.1181945319615184	-0.6360536807265150
0.1181945319615184	0.6360536807265150
0.1019301198172404	-0.7463319064601508
0.1019301198172404	0.7463319064601508
0.0832767415767048	-0.8391169718222188
0.0832767415767048	0.8391169718222188
0.0626720483341091	-0.9122344282513259
0.0626720483341091	0.9122344282513259
0.0406014298003869	-0.9639719272779138
0.0406014298003869	0.9639719272779138
0.0176140071391521	-0.9931285991850949
0.0176140071391521	0.9931285991850949